Virtual Design of Masonry Triplet Shear Tests using Digital Image Correlation

Louis Collin, Fabrice Gatuingt, Cédric Giry, François Hild

Virtual Design of Masonry Triplet Shear Tests using Digital Image Correlation

Louis Collin[1,2*], Fabrice Gatuingt[1†], Cédric Giry[1,3†], François Hild[1†]

[1*]Université Paris-Saclay, CentraleSupélec, ENS Paris-Saclay, CNRS LMPS - Laboratoire de Mécanique Paris-Saclay, Gif-sur-Yvette, France.
[2]ERMES, EDF R&D, Palaiseau, France.
[3]EPF École d'Ingénieurs, Cachan, France.

*Corresponding author(s). E-mail(s): lcollin@ens-paris-saclay.fr;
Contributing authors: fabrice.gatuingt@ens-paris-saclay.fr;
cedric.giry@ens-paris-saclay.fr; Francois.HILD@ens-paris-saclay.fr;
†These authors contributed equally to this work.

Abstract

Numerous studies highlight the diverse opportunities offered by multi-view image correlation techniques. For example, in masonry structures, these techniques enable the propagation of cracks to be quantified in joints and blocks. However, many parameters must be considered to transition from measurements to identifying physical parameters. Consequently, it is difficult to know *a priori* whether the planned experiment will enable for a precise identification of the model parameters to be calibrated. A good practice, detailed in this article, involves designing the experiment through virtual tests. The first step involves positioning the cameras in a virtual setup using Blender by combining near-field and far-field cameras for multiview purposes. Once a numerical model has been selected for nonlinear simulations, the second step involves examining the influence of geometric parameters to optimize the specimen response with respect to the quantities of interest. Last, virtual tests are conducted in Blender to simulate experiments under conditions close to reality. Based on the force data produced by the numerical simulations and the displacement fields measured from images generated during virtual tests, the proposed method enables for sensitivity analyses and uncertainty quantifications to ensure that the model parameters can be calibrated prior to the actual experimental campaign.

Keywords: test-computation dialogue, masonry, digital-image correlation, nonlinear response, uncertainties

1 Introduction

The behavior of masonry structures is heterogeneous, and cracking occurs typically within mortar joints [1, 2]. Characterizing the mechanical behavior at the joint level presents a significant challenge. Several traditional experiments for unreinforced or reinforced masonry have been developed at various scales, including the triplet shear test [3–8], the diagonal compression test on a panel [8–10], and in-plane loading of a masonry wall [9, 11–13], with the latter allowing for the consideration of openings [14, 15]. This paper focuses exclusively on the shear testing of a masonry triplet, following the EN 1052-3 standard [16]. In this test (Figure 1a), a force F is applied to the central block, while the two outer blocks are supported by simple bearings, with varying confinement levels σ applied through horizontal steel rods. The purpose of the tests is to estimate the shear strength as a function of the transverse confinement stress and to investigate the failure surface at mortar-brick interfaces. The influence of the three geometric parameters depicted here will be analyzed in Section 3 of this paper. The experimental setup, shown in Figure 1b, also facilitates the study of the cyclic shear response [6, 7]. In this configuration, it is important to note that vertical bars are necessary, but they may pose challenges for image acquisition.

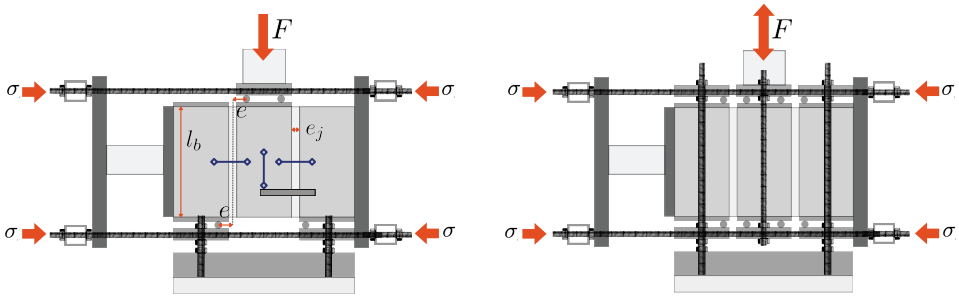

(a) Monotonic loading (b) Cyclic loading

Fig. 1: Experimental set-up for both monotonic (a) and cyclic (b) loadings

A conventional instrumentation for triplet shear tests involves two Linear Variable Differential Transformers (LVDTs) to record the relative shear displacement between the external and central units, and another LVDT to measure the vertical displacement of the central brick, as illustrated in blue in Figure 1a [4, 8, 17]. Although practical, this macroscale method only captures data at a specific point on the interface, which may not fully represent the heterogeneous shear distribution along the entire interface.

To overcome this limitation, full-field measurement techniques, such as digital image correlation (DIC), provide a more comprehensive analysis.

The first application of DIC to study displacement and strain fields at a stone/-mortar interface was introduced by Raffard et al. [18], while Shih et al. [19] used this technique for crack observation. Shortly thereafter, Réthoré et al. [20] applied DIC to capture shear band-like discontinuities similar to those occurring in masonry structures and to determine the geometry of the discontinuity line from the equivalent strain map. As a result, the authors successfully identified the frictional interface where shear occurred without reducing the size of the mesh and inherently raising the uncertainties.

Further validation of DIC measurements was first reported by Ghorbani et al. [12], who successfully compared DIC data with sensor readings during experiments on masonry infill walls, demonstrating comparable accuracy. Bolhassani et al. [21] obtained similar results focusing on bed-joint shear tests, diagonal compression, and in-plane shear tests. An interesting observation from the shear tests was the significant discrepancy between DIC and sensor data at the beginning of the test. This discrepancy decreased as the test progressed, which was attributed to the initial low strain levels. This observation indicates that DIC measurements require a minimum threshold of strain or displacement to yield reliable results. Therefore, experimental campaigns must be carefully planned to account for measurement uncertainties.

Based on the previous validations, Bompa et al. [5] employed DIC to create virtual gauges at the LVDT positions during triplet shear tests (Figure 1a) in order to monitor the relative displacement between the central brick and the lateral bricks. DIC data were also used to investigate post-peak crack patterns. Similarly, Thamboo et al. [3] used DIC measurements to characterize the strain state of samples, with particular focus on the unit–mortar interface. By plotting the shear stress versus the shear strain, the authors were able to determine the secant shear modulus.

For other masonry tests, Sciuti et al. [13] proposed a robust methodology to improve the accuracy of the measurements near cracks, including mesh adaptation and lower mechanical regularisation for damaged elements. Korswagen et al. [15] employed DIC to validate and calibrate non-linear finite element models. All these previous studies highlight the advantages of using DIC as a full-field measurement technique for triplet shear tests and propose robust methodologies to enhance the reliability of the measurements.

At this stage, it is important to note that other types of full-field measurement techniques are also available and have already been applied to masonry specimens. Binda et al. [22] used Electronic Speckle Pattern Interferometry (ESPI) to measure deformability characteristics in solid masonry units. Petry and Beyer [17] employed an optical measurement system consisting of two sensors, each with three cameras and LEDs attached to the masonry wall, comparing its performance to conventional measurement methods. Livitsanos et al. [23] and Peng et al. [24] monitored the fracture in masonry specimens by combining Acoustic Emission (AE) with Digital Image Correlation (DIC), offering a comprehensive approach to such analyses.

Most of the time, only 2D measurements were reported when studying masonry triplets [3, 5]. However, Ghorbani et al. [12] reported a pilot study testing the use of

stereocorrelation (or 3D-DIC), which allows the quantification of both in-plane and out-of-plane motions. This capability is crucial for validating the assumption of purely in-plane loading. In relation to boundary condition considerations, Fedele et al. [25] emphasized the importance of using experimentally measured boundary conditions from DIC for accurate calibration of mechanical parameters. Another interesting approach introduced by Hamadouche et al. [26] involves the use of an additional camera to zoom in on a specific area with higher resolution, as demonstrated on a notched three-point bending specimen. This multiview correlation (M-DIC) technique reduces the measurement uncertainties within the region of interest and is particularly beneficial for masonry triplets, where crack patterns are often predictable within the mortar joints. A multiview system that allows for 3D-DIC is highly relevant for improving measurement accuracy during triplet shear tests. However, it requires a substantial number of cameras and results in a more complex experimental setup.

Such comprehensive full-field datasets are invaluable for validating nonlinear models and scaling up to full-scale simulations. Finite Element Model Updating (FEMU), first introduced by Kavanagh and Clough [27], uses an iterative procedure to compare measured and simulated displacement, strain, or load levels [28]. The coupling of DIC with FEMU has been studied by Leclerc et al. [29], and numerous works in the mechanical field have demonstrated its robustness. For instance, in the Digital Volume Correlation field, Turpin et al. [30] applied this approach to study damage of a composite material subjected to multiaxial loading. In contrast, Vargas et al. [31] used it to calibrate cohesive parameters in castable refractory materials.

Like any measurement tool, DIC has inherent uncertainties. Bornert et al. [32] proposed a general procedure to assess DIC displacement measurement errors. To address the uncertainties associated with this method, Roux and Hild [33] provided insights into how image noise propagates through DIC and identification procedures such as FEMU, thereby allowing the uncertainty of each identified parameter to be quantified.

The work proposed herein is the first step of an upcoming experimental campaign on triplet shear tests that will involve multiview DIC measurements followed by parameter identification using FEMU. Implementing these tests is both time-consuming and complex, requiring attention to several factors, such as the design of an appropriately sized speckle pattern, the positioning of cameras, and an optimized lighting setup. Moreover, the nonlinear models that are planned to be used rely on numerous parameters and internal variables that must be precisely identified throughout the experimental campaign. Consequently, this work seeks to establish a robust test-simulation dialogue, bridging numerical simulations with experimental campaigns before and after testing. A recent article [34] briefly discusses a general methodology for this approach.

This paper aims to propose a novel methodology to assist experimentalists in preparing complex test campaigns. This approach draws inspiration firstly from the work of Rouzaud et al. [35], who examined the influence of experimental parameters on the dynamic response of reinforced concrete (RC) structures through parametric analyses using the Taguchi Method [36]. Their work enables experimentalists to design testing parameters that impact the simulated response. Similarly, Vitse et al. [37]

optimized tests on reinforced concrete beam-column joints by simulating a multi-view system within the Blender animation software and generating realistic specimen images, facilitating the determination of sensitivity fields.

The novelty of this work lies in combining both approaches and extending the process to include virtual tests using Blender, M-DIC calculations on the generated virtual images, as well as sensitivity analyses relevant to FEMU. This procedure enables *a priori* to assess whether each parameter of the nonlinear model can be accurately calibrated and with what level of uncertainty. It finally validates using M-DIC for civil engineering applications, such as masonry.

Section 2 provides an overview of the pinhole camera model, followed by an examination of how camera positioning affects the design of the vision setup. In Section 3, the preliminary finite element modeling approach for the triplet shear test is briefly introduced, focusing on the design of the specimen's geometry through a parametric analysis. Section 4 presents the equations for both monoview and multiview DIC, followed by the virtual testing approach and the results of the virtual experiments. This study is followed by a sensitivity analysis, uncertainty quantification, and a discussion on designing an optimal speckle pattern for enhanced measurement resolution.

2 Design of the camera set-up

2.1 Pinhole camera model

Let us consider a point in the scene $\mathbf{X} = [X \ Y \ Z]^T \in \mathbb{R}^3$ defined by its 3D-coordinates in the object frame R. Through the pinhole model for each camera $^{(c)}$, the 2D-coordinates of this point $\mathbf{x^{(c)}}$ in the image frame $R^{(c)}$ can be determined [38]

$$\begin{Bmatrix} x^{(c)} \\ y^{(c)} \\ 1 \end{Bmatrix} = [\mathbf{K}^{(c)}] \ [\mathbf{\Theta}^{(c)} \ , \mathbf{t}^{(c)}] \ \begin{Bmatrix} X \\ Y \\ Z \\ 1 \end{Bmatrix} \tag{1}$$

The global matrix $[\mathbf{K}^{(c)}] \ [\mathbf{\Theta}^{(c)} \ , \mathbf{t}^{(c)}]$, known as the projection matrix $[\mathbf{\Pi}^{(c)}]$, is used to map a point coordinates from 3D space to the 2D image plane. The parameters in matrix $[\mathbf{K}^{(c)}]$ are denigrated as intrinsic parameters, while the geometric parameters contained within $[\mathbf{\Theta}^{(c)}, \mathbf{t}^{(c)}]$ are denigrated as extrinsic. These parameters are identified during the calibration phase [38]. In virtual experiments, the projection matrix is known since the elements of the experimental setup are precisely positioned in the 3D space and parameterized with their intrinsic values.

2.2 First approach for camera set-up design

An initial question involves positioning the cameras to focus on the critical areas that need careful monitoring. When testing masonry triplets, cracks are expected to develop in one or both masonry joints. To investigate the effect of camera positioning, a Python code was developed to simulate the projection process described above. Each camera is defined by the position of its optical center $(X_c^{(c)}, Y_c^{(c)}, Z_c^{(c)})$ and the orientation

of the image frame $R^{(c)}$, with a rotation angle $\theta_Z^{(c)}$ about the plane's normal. This normal is determined by the optical center and the target point with coordinates $(X_t^{(c)}, Y_t^{(c)}, Z_t^{(c)})$ (Figure 2). This process fully defines the matrix $[\mathbf{\Theta}^{(c)}, \mathbf{t}^{(c)}]$ for each camera. Additionally, each one is characterized by its focal length $f^{(c)}$ and sensor dimensions $(s_x^{(c)}, s_y^{(c)})$. This setting allows one to define the values of $f_x^{(c)}$ and $f_y^{(c)}$. The optical center coordinates are assumed to be $u_0^{(c)} = v_0^{(c)} = 0$. Last, the aperture is selected to set the depth of field for each camera.

$$[\mathbf{K}^{(c)}]\ [\mathbf{\Theta}^{(c)}\ ,\ \mathbf{t}^{(c)}]\ =\ \begin{pmatrix} f_x^{(c)} & 0 & 0 \\ 0 & f_y^{(c)} & 0 \\ 0 & 0 & 1 \end{pmatrix} \begin{pmatrix} \mathbf{\Theta}^{(c)} & \mathbf{t}^{(c)} \\ \mathbf{0}^T & 1 \end{pmatrix} \tag{2}$$

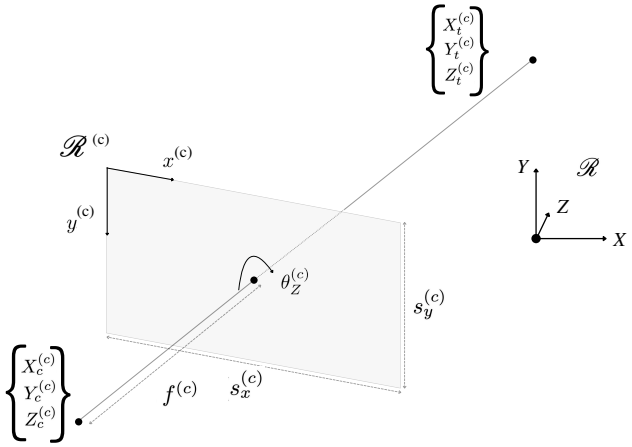

Fig. 2: Schematic drawing of the pinhole camera model with the hardware parameters

By implementing this projection sequence, one can analyze how specific variables, such as coverage, change in a test [26, 34, 37], depending on the camera positions and parameters described in Table 1. In the present setup, three far-field cameras are employed to monitor all the specimen surfaces. Camera 1 is used to perform 2D-DIC, while Cameras 2 and 3, positioned at different observation angles, enable 3D-DIC measurements. Additionally, a fourth near-field camera, rotated by 90° relative to the others, focuses on the left mortar region to provide improved tracking of crack development in that area. This vertical orientation was selected to capture a larger mortar area than would be possible with a horizontal setup. The combined use of the four cameras enables multiview and multiscale instrumentation (M-DIC). A comparison between these different configurations (2D-DIC, 3D-DIC, and M-DIC) is proposed in Section 4.3.

Table 1: Hardware parameters

	Camera 1	**Camera 2**	**Camera 3**	**Camera 4**
Lens $f^{(c)}$ (mm)	24	24	24	65
Aperture	$f/2.8$	$f/2.8$	$f/2.8$	$f/2.8$
Sensor size ($s_x^{(c)}$; $s_y^{(c)}$) (mm ; mm)	$(23,5\ ;\ 15,6)$	$(23,5\ ;\ 15,6)$	$(23,5\ ;\ 15,6)$	$(23,5\ ;\ 15,6)$
$X_c^{(c)}$ (m)	0	0.25	-0.25	-0.1
$Y_c^{(c)}$ (m)	0.82	0.82	0.82	0.92
$Z_c^{(c)}$ (m)	1.0	1.0	1.0	1.0
$\theta_Z^{(c)}$ (°)	0	0	0	90
$X_t^{(c)}$ (m)	0	0	0	-0.1
$Y_t^{(c)}$ (m)	0.82	0.82	0.82	0.92
$Z_t^{(c)}$ (m)	0	0	0	0

The main advantage of this modeling is the ability to plot a coverage map on the specimen surface, indicating how many cameras observe each point on the tested piece (Figure 3a). This visualization helps confirm that the cameras still observe areas that elements of the setup may otherwise obscure. The focus is on the cyclic triplet shear test, which involves vertical bars that may interfere with image acquisition (Figure 3b). The results from the simulation show that at least one camera captures each point in the region of interest, which is satisfactory. The coverage maps illustrate the multiview and multiscale approach, with Camera 4 capturing only a specific specimen region.

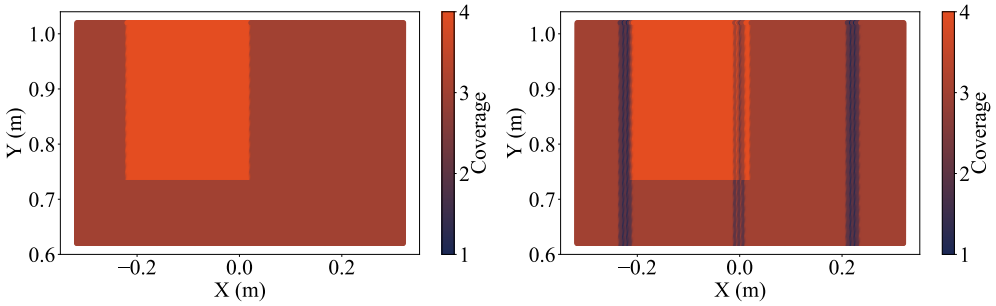

(a) Monotonic loading

(b) Cyclic loading

Fig. 3: Coverage map for the monotonic (a) and cyclic (b) triplet shear tests with the camera setup defined in Table 1)

2.3 Virtual design

An initial advantage in implementing the virtual design of an experiment is the ability to create a precise digital model of the test area, enabling the definition and validation of all used components [37, 39]. In the case of shear tests, all components comprising the supports and the pre-tensioning system were initially imported into Blender, an

open-source animation and visualization software [https://www.blender.org/]. Figure 4a shows the view of both experimental set-ups.

Figure 4b shows that the horizontal bars intended for confinement interfere with image acquisition. Therefore, the components were adjusted before machining to ensure they did not interfere again. Additionally, Blender facilitated the configuration of the camera setup and lighting to be used during the experiment. The software allows for positioning cameras in the scene with various intrinsic and extrinsic parameters described previously.

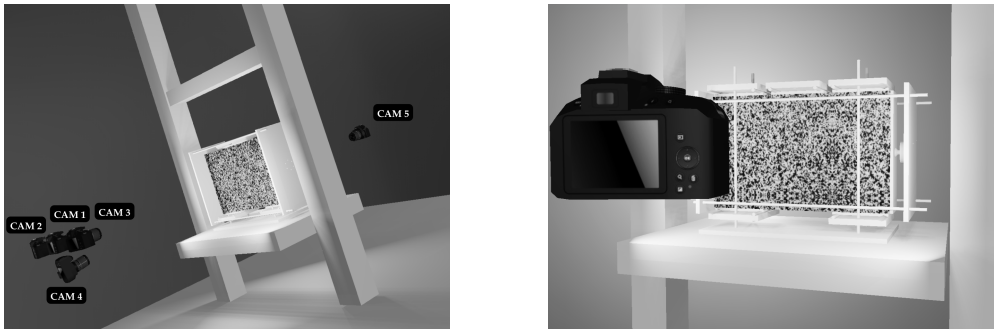

(a) (b)

Fig. 4: (a) Final experimental set-up for triplet shear tests. (b) Some bars obstruct image acquisition.

Different types of lighting can also be added and set. This feature enables the creation of realistic renderings of the experiment (Figure 5) and allows for the pre-estimation of the positioning of all necessary equipment suitable for image correlation.

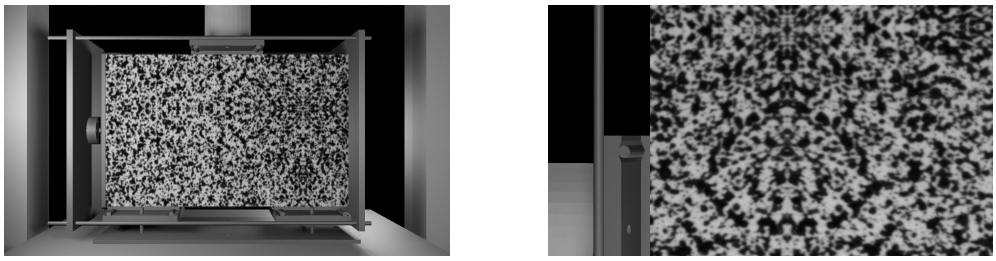

(a) Camera 1 (b) Camera 4

Fig. 5: Virtual images acquired by cameras 1 and 4

Table 2 provides the cameras' positions in space, with the specimen surface of interest located at coordinate $z = 0$, and the intrinsic parameters, respectively. The

developped Python code also allows for pre-positioning the cameras in the Blender scene. In practice, the camera positions listed in Table 2 were used as initial targets during the experimental campaign, significantly reducing the setup time for the complex multiview measurement system. The primary interest of virtual design therefore lies in the preparation and implementation of the experimental setup [37]. The proposed work seeks to go further by optimizing the design of the specimen and carrying out a sensitivity analysis on the entire experimental chain modeled on Blender, based on the results of a numerical model.

Table 2: Cameras parameters for virtual triplet shear tests

	Camera 1	**Camera 2**	**Camera 3**	**Camera 4**
Lens $f^{(c)}$ (mm)	25	25	25	60
Aperture	f/8	f/8	f/8	f/8
Sensor size ($s_x^{(c)}$; $s_y^{(c)}$) (mm ; mm)	(23.5 ; 15.6)	(23.5 ; 15.6)	(23.5 ; 15.6)	(23.5 ; 15.6)
Definition (px ; px)	(6000 ; 4000)	(6000 ; 4000)	(6000 ; 4000)	(6000 ; 4000)
$X_c^{(c)}$ (m)	-1.15	-1.15	-1.15	-1.1
$Y_c^{(c)}$ (m)	0.	-0.25	0.25	-0.1
$Z_c^{(c)}$ (m)	0.82	0.82	0.82	0.70
$\theta_Z^{(c)}$ (°)	0	0	0	90

3 Design of specimen geometry through parametric analysis

The objective in designing the specimen geometry is to ensure that the behavior during tests is such that the DIC system is sensitive enough to provide meaningful data. Specifically, the goal is to track the nonlinear response over the broadest possible range, avoiding an overly brittle behavior. The model, which serves as a necessary assumption, is first presented to provide a basis for the analysis.

3.1 Description of the model

3.1.1 Geometry

The masonry triplets are made of three solid concrete blocks, with initial dimensions of $40 \times 20 \times 10\,\mathrm{cm}^3$. Joints connect these blocks with a thickness ranging between 2 and 3 cm. This section examines the influence of some of these parameters on the force-displacement response, particularly the block length l_b and the joint thickness e_j. The hinged supports at the top and bottom are placed symmetrically with respect to the centre of the joint at a distance e (Figure 1a).

3.1.2 Nonlinear constitutive model

Triplet shear tests are simulated using the Finite Element Code Cast3M (https://www-cast3m.cea.fr/). The objective is to analyze the behavior of mortar elements at

a microscale. A conventional approach typically involves replacing mortar with joint elements or modeling contact at the interface between blocks [40, 41]. However, in the present case, the aim is to use measured displacement fields as input to calibrate material parameters. For this reason, detailed modeling of mortar is preferred [6, 7, 42]. It is also worth noting that Andreotti et al. [4] employed both a continuous model for the blocks and mortar while incorporating joint elements at the interface.

During a triplet shear test, damage typically occurs at the interface between mortar and the masonry unit, inside mortar through shear failure, or, less frequently, within the masonry units themselves. Once the crack propagates from top to bottom, friction due to sliding is observed on either side of the crack, which depends on the level of confinement [5–7]. For cyclic loading, hysteresis loops are observed on the force-displacement curve, which indicates energy dissipation [6, 7].

The mortar between masonry units is represented using finite elements and modeled with an isotropic damage model that includes friction and unilateral effects. The nonlinear model developed by Vassaux et al. [43, 44] is selected for this study due to its well-established ability to describe the cyclic behavior of quasi-brittle materials such as concrete. Since the studied masonry is composed of solid concrete blocks and cement with mechanical properties similar to those of concrete, this modeling choice was deemed appropriate. The detailed equations for this model are provided in the Appendix A for reference.

These mortar elements possess elastic and quasi-brittle features, as outlined in Table 3. Further details on these parameters can be found in Refs. [43, 44]. The quantities E_j and ν_j are the Young's modulus and Poisson's ratio, respectively (the index j stands for joint, and b for block). Introducing nonlinearity involves terms such as $\sigma_{t,j}$ for the damage stress, $a_{tra,j}$ for the damage law evolution, q_{pj} governing for the crack closure rate, and $c_{f,j}$ for friction at the crack level (Appendix A) . The parameter values are determined from the results of individual characterization tests (for E_j, ν_j, and $\sigma_{t,j}$), as well as from a range of available test cases for the model [43, 44]. Concurrently, the block elements are assumed to remain elastic (Table 3).

Table 3: Mechanical parameters for mortar

	E_j	ν_j	$\sigma_{t,j}$	$a_{tra,j}$	$q_{p,j}$	$c_{f,j}$
Material	Pa	/	Pa	$\mathrm{kJ}^{-1} \cdot \mathrm{m}^3$	/	/
Mortar	22×10^9	0.19	8.4×10^5	4×10^{-3}	6.5	2.89
Block	40×10^9	0.2	/	/	/	/

To ensure a uniform density at the joint level, the entire structure has been meshed using cubic elements with linear interpolation functions, each with dimensions of approximately $0.7 \times 0.7 \times 0.7$ cm^3. This configuration results in three cubic elements spanning the thickness of the 2 cm joints. This mesh will also be used for the DIC calculations once the experiments are completed and, therefore, represents a compromise between having an element size fine enough to capture crack propagation in mortar joints and large enough to avoid excessive measurement uncertainties. In the final stage for the monotonic loading, a displacement ranging from 0 to 0.1 mm is applied

to the central block, in line with similar internal tests conducted on comparable specimens. The displacements of the end blocks are numerically constrained at the hinges. Additionally, a uniform normal stress σ_p is applied to both lateral surfaces to represent the confinement prescribed on masonry blocks in larger structures.

3.1.3 Simulation results

The simulation results are shown in Figure 6 for the parameter sets described in Table 3, corresponding to monotonic and cyclic loadings. An initial elastic phase is observed, followed by a nonlinear behavior until the breaking force is reached. The model has been validated through internal tests (Figure 6b) in terms of displacement and peak load. The next step involves optimizing the sample geometry through a parametric study to ensure that the specimen response aligns with the sensitivity range of the measurement devices.

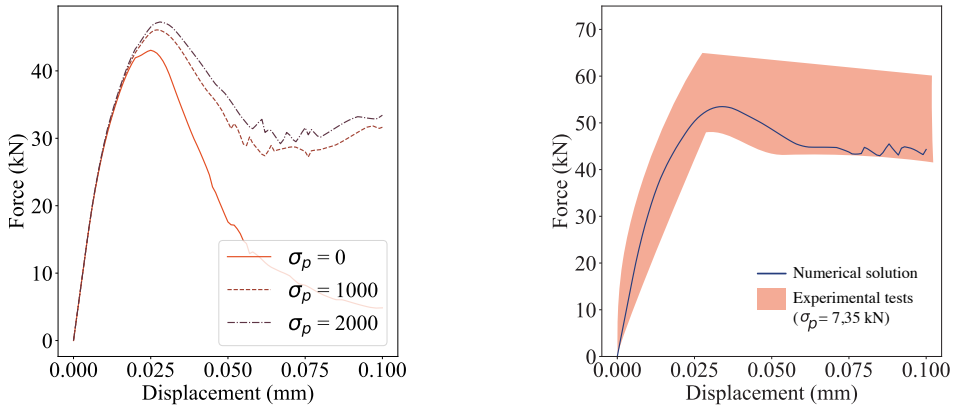

(a) Monotonic loading

(b) Numerical validation

Fig. 6: Force-displacement curves for monotonic loadings (a) and validation through internal tests (b)

3.2 Design of specimen geometry

The modelling outlined benefits from sensitivity analysis to better understand how geometric parameters affect the response in triplet shear tests. This analysis is valuable since the experimental setup had to be constructed from scratch. This approach is similar to Design of Experiments (DOEs), which involves planning, executing, and analyzing controlled tests to evaluate how various factors influence key parameters. This method is commonly used in industrial design to optimize parameters for achieving the desired product specification, though its cost depends on the number and complexity of the required tests.

Rouzaud et al. [35] proposed using virtual experiments to perform DOEs. For triplet shear tests, the primary objective is to maximize the nonlinear phase. This condition is quantified by a parameter Δu_{nl}, representing the difference between the displacement at peak load and the first displacement at which the simulated force deviates from what is expected in the elastic regime. This offset helps avoid overly brittle responses. Furthermore, achieving a sufficiently large displacement at failure u_{peak} is crucial, as a failure at minimum displacement would reduce the interest of DIC. Similarly, the peak force F_{peak} must align with the sensor measurement range. Therefore, the aim is to determine the optimal geometric parameters that maximize these three quantities of interest, ensuring accuracy and robustness in the test.

3.2.1 First parametric analysis

The parametric analysis using a one-at-a-time strategy [45] focuses on understanding the impact of key geometric parameters—joint thickness (e_j), block length (l_b), and support position (e)—on the force-displacement response in triplet shear tests. The numerical results of these analyses are presented in appendix B. They reveal that increasing the joint thickness leads to a more significant post-failure force drop, while the block length affects the force and displacement at failure. The support position does not significantly influence the test outcome when varying within the recommended range [16].

3.2.2 Application of Taguchi Method [36]

The first parametric analysis investigated the individual influence of each geometric parameter on the quantities of interest. The next step is to determine the optimal combination of these parameters. The remaining parameters to vary are the following within the specified range of discrete values :

- Joint thickness: $e_j = 2$; 3 cm;
- Block length : $l_b = 30$; 40 cm;
- Support position : $e = 2$; 3 cm

The DOEs are categorized into two main types: full and reduced plans. Using a simplified Taguchi sensitivity analysis with variables set at two levels, one can minimize the number of tests to just four instead of the original eight tests (2^3). This property results in substantial time savings during the virtual campaign [35], mainly if the number of geometric parameters to be studied increases.

Table 4: Taguchi table L3 and results

Tests	e_j (cm)	l_b (cm)	e (cm)	F_{peak} (kN)	u_{peak} (mm)	Δu_{nl} (mm)
1	2	30	2	38.1	0.024	0.019
2	2	40	3	46.1	0.028	0.023
3	3	30	3	40.7	0.026	0.019
4	3	40	2	43.7	0.033	0.028

This method directly provides the test sequence to be computed (Table 4). Once these virtual tests are completed (Figure B1d), the results are used to determine the effect of each parameter. To accomplish this task, statistical techniques are based on the property of orthogonality [35]. The effect E of a factor x_i at a level A_i is defined as

$$E(x_i) = \bar{M}(x_i = A_i) - \bar{M}(x_i) \tag{3}$$

where $\bar{M}$ is the mean of the measured quantities.

Table 5: Effects of the geometric parameters on the three quantities of interest

Parameter	**Levels**	$E(F_{\text{peak}})$ (kN)	$E(u_{\text{peak}})$ (μm)	$E(\Delta u_{\text{nl}})$ (μm)
Joint thickness	2 cm	-0.05	-2.0	-1.25
	3 cm	0.05	2.0	1.25
Length block	30 cm	-2.76	-3.0	-3.25
	40 cm	2.76	3.0	3.25
Support position	2 cm	-1.23	1.0	-1.25
	3 cm	1.23	-1.0	1.25

At this point, one concludes that the block length significantly influences the three quantities of interest with the highest effect (Table 5). Conversely, the joint thickness primarily affects the displacement at failure (Table 5). At the same time, the distance between the supports has a relatively minor effect compared to the previous two parameters (Table 5). For the investigated tests, considering the maximum width constraint of the testing machine, the following set of parameters are selected:

- Joint thickness: $e_j = 2$ cm;
- Block length: $l_b = 40$ cm;
- Support position: $e = 2$ cm.

This approach is expected to maximize the peak force while ensuring a sufficiently large displacement during the non-linear regime and at peak, which is crucial given the uncertainties in DIC measurements. The non-linear phase will also be extended enough to enable effective crack quantification throughout the test. These first results are particularly interesting when considering the uncertainties related to the three geometrical parameters in real-world conditions. The concrete blocks are to be cut with a circular saw and measured before each fabrication of the triplet. The average length is $l_b = 40.06$ cm with a standard deviation of 0.08 cm (based on 24 specimens) . In contrast, controlling the joint thickness during triplet fabrication is much more complex, and accurately measuring it afterwards is not easy. The parameter e_j will thus vary more significantly, ranging between 1.8 and 2.2 cm. Based on the previous results, this variability should have a real impact on the measurements. Finally, since the parameter e is specific to the experimental setup, it will not change but will require precise specimen centring.

4 Virtual testing and sensitivity analyses using Blender

The previous sections aimed to better understand the model's geometric parameters and provide an initial proposal for camera placement. The idea is now to enrich the approach through virtual testing. Generating virtual images of the deformed specimen allows for DIC calculations, whose results are used in a sensitivity analysis to assess the identifiability of various parameters. Ultimately, this process helps to assess uncertainties and optimize experimental parameters such as speckle size.

4.1 Multiview correlation

The innovation in the experiments to be conducted involves using multi-view systems. When studying heterogeneous materials like masonry specimens, having multiple cameras that monitor various resolutions and specific sections of the tested structures is crucial [25]. The measurement uncertainties in DIC depend on factors such as element size in global approaches. Larger elements contain more pixels for a given resolution, resulting in lower measurement uncertainties. However, capturing steep displacement gradients or discontinuities, especially at masonry joints, requires fine meshes, which increase measurement uncertainties [13, 46].

Passieux et al. [47] introduced a near-field/far-field DIC approach to address this challenge. This method used two cameras with different resolutions, one capturing images of the entire sample surface (far-field) and the other zooming in on a smaller area (near-field). These near-field and far-field analyses were treated independently, and a multi-scale transformation was used to register the reference images. This approach effectively reduced measurement uncertainties. Subsequently, Hamadouche et al. [26] developed a unified framework that integrates multiview approaches across different scales to improve the use of redundant data from areas monitored by multiple cameras. The results of a three-point bend test performed on a concrete beam show that the proposed method reduces the associated displacement uncertainties. Damage initiation and propagation can then be successfully quantified.

Monoview image correlation relies on the gray level conservation [46] for each pixel,

$$\forall \mathbf{x} \in R, f(\mathbf{x}) = g(\Phi_0(\mathbf{x})) = g(\mathbf{x} + \mathbf{u}(\mathbf{x})) \tag{4}$$

where $R \subset \mathbb{R}^2$ denotes the Region of Interest (ROI), f and g the reference and deformed images respectively, and Φ_0 denotes the sought mechanical transformation. In this context, the sum of squared differences reads

$$C_1 = \int_R [f(\mathbf{x}) - g(\mathbf{x} + \mathbf{u}(\mathbf{x}))]^2 \mathbf{dx} \tag{5}$$

The DIC cost function, Φ_c^2, can be defined with σ_c as the standard deviation of acquisition noise (of camera c), which is assumed to be white and Gaussian

$$\Phi_c^2 = \frac{1}{2\sigma_c^2} C_1 \tag{6}$$

When using multiple cameras (e.g., stereo-correlation (3D-DIC) techniques [12, 38, 48]) if there are no variations in brightness and contrast, the gray levels on the sample surface should appear consistent for all N_c cameras [38]. Consequently, it is possible to create an intrinsic pattern $\hat{f}(\mathbf{X})$ of the speckle pattern for all physical points [48]. This pattern is defined as the average gray level of the images, $f^{(c)}(\mathbf{x}^{(c)})$, for all cameras

$$\hat{f}(\mathbf{X}) = \frac{1}{N_c} \sum_{c}^{N_c} f^{(c)} \left(\mathbf{x}^{(c)} \left([\mathbf{\Pi}^{(c)}], \mathbf{X} \right) \right) \tag{7}$$

Minimizing the cost function for each camera must account for the region of interest $R^c \subset R$ specific to each camera c. The global M-DIC cost function for N_c cameras can be formulated as

$$\Phi_{M-DIC}^2 = \sum_{c=1}^{N_c} \frac{1}{2\sigma_c^2} \int_{R^{(c)}} \left(\hat{f}(\mathbf{X}) - f_{\mathbf{U}}^{(c)} \left(\mathbf{x}^{(c)} \left(\mathbf{\Pi}^{(c)}, \mathbf{X} \right) \right) \right)^2 d\mathbf{X} \tag{8}$$

where $f_{\mathbf{U}}^{(c)} \left(\mathbf{x}^{(c)} \left(\mathbf{\Pi}^{(c)}, \mathbf{X} \right) \right)$ represents the corrected deformed image the c-th camera recorded at time t.

The displacement field $\mathbf{u}$ is sought as a linear combination of a set of spatial shape functions $\mathbf{\Phi}_i$

$$\mathbf{U}(\mathbf{X}) = \sum_{i}^{N_n} a_i(t) \mathbf{\Phi}_i(\mathbf{X}) \tag{9}$$

where $\{\mathbf{a}(t)\}$ stands for the nodal displacement to be determined at each time instant t. At each iteration, a Gauss-Newton Scheme gives the correction $\{\delta\mathbf{a}\}$ computed from the linear system [38]

$$[\mathbf{M}_{DIC}]\{\delta\mathbf{a}\} = \{\mathbf{h}_u\} \tag{10}$$

$$\{\mathbf{a}(t)\} = \{\mathbf{a}(t)\} + \{\delta\mathbf{a}\} \tag{11}$$

where $[\mathbf{M}_{DIC}]$ is the DIC Hessian matrix, which is symmetric and non-negative by construction [49]. The applicability of a multiview system will be specifically addressed in Section 4.3, with a comparison to monoview and stereo configurations in terms of uncertainties and sensitivity. The multiview correlation framework is now applied to the virtual images generated using the Blender animation software, just as it would be in a real experiment.

4.2 Virtual testing

One of Blender's most significant capabilities is the ability to create virtual yet realistic images suitable for M-DIC calculations During virtual tests, the specimen and the applied speckle pattern (Figure 4a) are deformed according to the displacement fields $\mathbf{u}_{FE}(t)$, which are simulated at various time steps, hereafter referred to as index, using BlenDIC, an open-source Blender add-on [https://gitlab.com/sciviz/blendic].

The virtual setup allows for the measurement of these displacements through the configured multiview system described in Section 2.2 (Table 2) . Consequently, virtual images are generated, replicating the expected outcomes of real experiments (Figure 5). These virtual images can be analyzed using the M-DIC framework to measure displacement fields $\mathbf{u}_{DIC}(t)$.

A first virtual test is conducted on the triplet shear setup. The parameters used in Cast3m for the Finite Elements simulation to obtain $\mathbf{u}_{FE}(t)$ are those described in Table 3. For each camera, it is necessary to map the mesh onto the image. The projection matrices $[\mathbf{\Pi}^{(c)}]$ generated by Blender are used to accurately determine the coordinates of the mesh nodes (Figure 7). In practice, a margin of 10 pixels is left around the edges of the image to avoid edge-related errors in DIC calculations.

Table D2 summarizes the DIC hardware parameters for the four front cameras. The M-DIC calculation is then run [50], and the results for the final timestep after cracking are shown in Figure 8.

The observed results are consistent with the expected kinematics. Figure 8a reveals pronounced displacement gradients, indicative of cracks in the mortar along the specimen height. Figures 8b and 8c demonstrate that displacements along the $X-$ and $Z-$ directions are predominantly attributable to measurement noise, with no significant displacement detected. However, it is observed that noise levels in the $X-$ direction are reduced within the region of interest of camera 4, while noise levels in the $Z-$direction are comparatively higher. This result opens up the possibility of conducting a virtual testing campaign to perform an in-depth sensitivity analysis.

4.3 Identification of parameters through virtual testing

One of the novelties of the work presented herein lies in using the measured displacement fields $\mathbf{u}_{DIC}(t)$, obtained through M-DIC to perform a sensitivity analysis and *a priori* assess the identifiability of each parameter. A key advantage is that the displacement uncertainty γ_u reflects all sources of error in the measurement chain, including the speckle pattern, lighting, and optical setup, thanks to Blender's ability to parameterize the entire measurement process. This feature represents a significant strength in preparing (complex) experiments.

Several camera configurations are considered, namely, the 2D-DIC configuration (Camera 1), the multiscale configuration (Cameras 1+4), the 3D-DIC configuration (Cameras 2+3 or Cameras 1+2+3), and the M-DIC configuration (Cameras 1+2+3+4). The results presented below will highlight the advantages of the M-DIC configuration over the other setups, particularly in terms of reduced uncertainties and increased sensitivity in key areas.

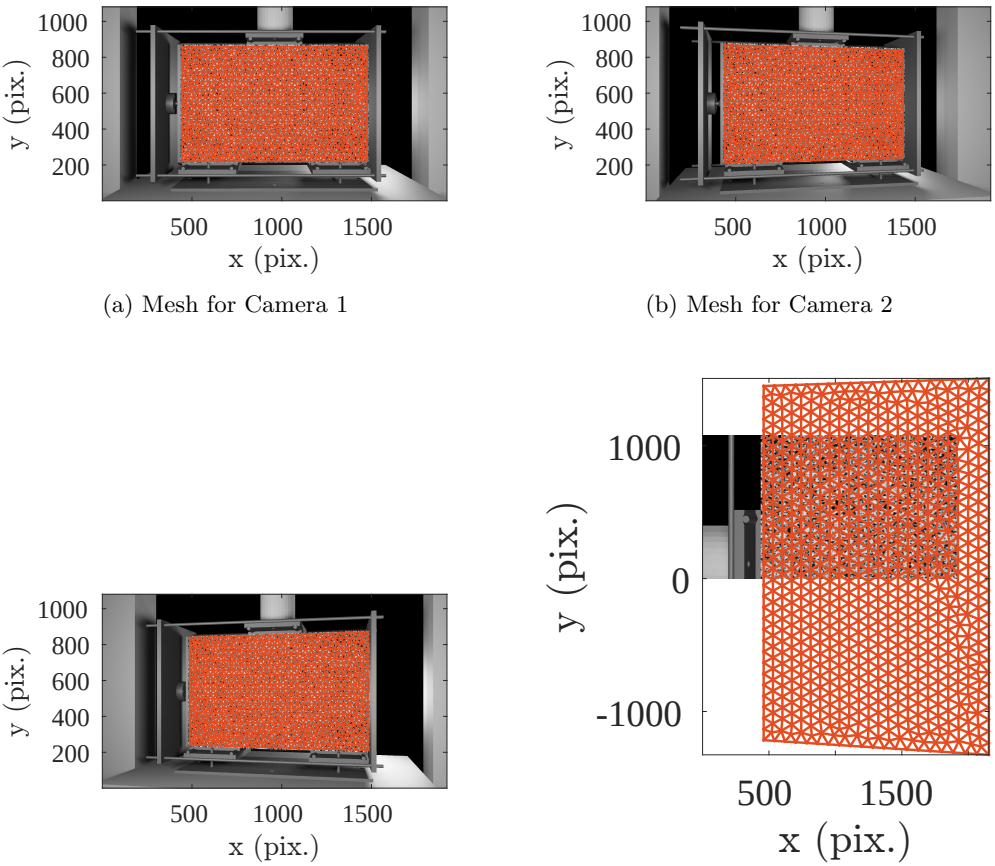

(a) Mesh for Camera 1

(b) Mesh for Camera 2

(c) Mesh for Camera 3

(d) Mesh for Camera 4

Fig. 7: Projected 3D mesh onto 2D sensor planes of Cameras 1 (a), 2 (b), 3 (c), and 4 (d).

The sensitivity analysis involves simulating the experiment with different parameter values to evaluate the measurement sensitivity to various characteristics, such as adjustments to optics, speckle, and lighting, while also considering potential measurement uncertainties. The approach proposed by Vargas et al. [31] is followed. Beginning with an initial set of parameters $\{\mathbf{p}_0\}$ and using a relatively fine mesh, additional simulations are conducted by increasing each parameter value by 1% (Table C1). The goal is to determine the impact of the six parameters listed in Table 3. As a result, seven simulations are run using Cast3M. Each simulation i produces a force-displacement curve and displacement fields $\mathbf{u}_{FE}^{(i)}$ for each time step.

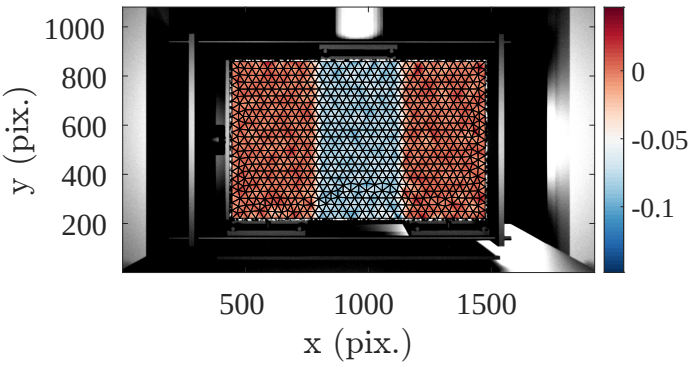

(a) Displacement field in the Y-direction.

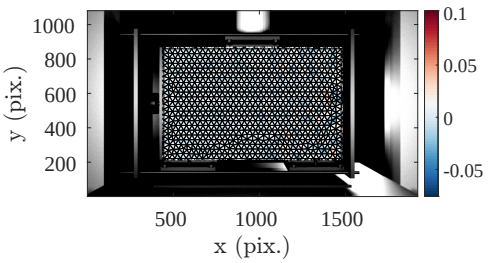

(b) Displacement field in the X-direction.

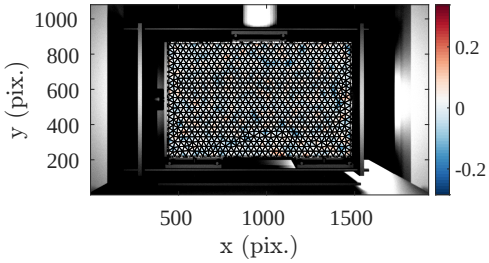

(c) Displacement field in the Z-direction.

Fig. 8: Displacement fields in mm measured through M-DIC: (a) in the Y-direction (vertical), (b) in the X-direction (horizontal) and (c) in the Z-direction.

4.3.1 Signal Noise to Ratio Level

Using these results, for each test i, two matrices are defined to provide the signal-to-noise Ratio (SNR) level, one for the force $\mathbf{F}$, and the other for the displacement field $\mathbf{u}_{FE}$. They are normalized by the standard measurement uncertainty, with γ_F and $\boldsymbol{\gamma}_u$ corresponding to force and displacement, respectively. These matrices are dimensionless and indicate, at each time step t, how many times the fluctuations vary with respect to the measurement uncertainty.

$$
\begin{aligned}
SNR_F^{(i)}(t) &= \frac{F^{(i)}(t,\{\mathbf{p}^{(i)}\}) - F^{(0)}(t,\{\mathbf{p}^{(0)}\})}{\gamma_F} \\
\{\mathbf{SNR}_u^{(i)}(t)\} &= \frac{\{\mathbf{u}_{FE}^{(i)}(t,\{\mathbf{p}^{(i)}\})\} - \{\mathbf{u}_{FE}^{(0)}(t,\{\mathbf{p}^{(0)}\})\}}{\{\boldsymbol{\gamma}_u\}}
\end{aligned}
\tag{12}
$$

where i is the index of the test (Table 3), also corresponding to the index of the parameter that varied compared to the initial test indexed as 0. First, the sensitivity curves for the force are shown in Figures 9 with a standard uncertainty $\gamma_F = 10$ N. Each curve is compared to the reference curve provided in appendix C2.

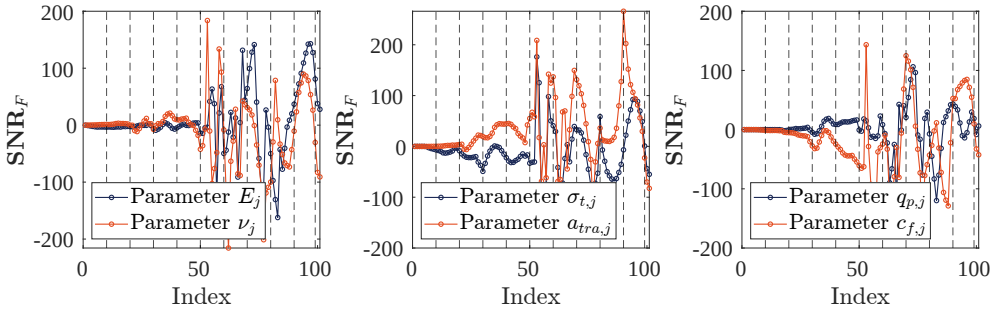

Fig. 9: Sensitivity curves $\mathbf{SNR}_F$ - Vertical dashed lines represent image time steps

The parameters E_j and ν_j are the only ones active during the elastic phase of the test (index 1 to 6). The tensile strength $\sigma_{t,j}$ is then activated once the elastic limit is exceeded, followed by the activation of the other parameters that govern the nonlinear response, $a_{tra,j}$, $q_{p,j}$, and $c_{f,j}$, at index 20. The six parameters reached sensitivities at least 50 times the uncertainty level at specific time steps. This result indicates that a 1% change in these parameters results in a sensitivity 50 times greater than the force measurement uncertainty, ensuring that the precise identification of these parameters is minimally affected by measurement uncertainty. After index 50, the residual regime is reached, characterized by a more disorganized evolution of $\mathbf{SNR}_F$ and higher values.

Regarding the standard uncertainty in displacement measurements, unlike real-world tests where noise from measurement devices is inevitable, virtually generated images are noise-free. However, BlenDIC allows the introduction of noise to these images. In this study, a white noise was added with a mean value of 0 and a standard deviation σ^2 of 2 gray levels. Three camera configurations were analyzed, namely Cameras 2+3, Cameras 1+2+3, and Cameras 1+2+3+4. An initial calculation was conducted on 10 noisy images in the reference configuration [31], from which the standard displacement uncertainty $\boldsymbol{\gamma}_u$ fields for 3D-DIC and M-DIC configurations (Figure D3) were determined. The results show that increasing the number of cameras used to monitor the specimen leads to a reduction in the standard uncertainty. The average value of $\boldsymbol{\gamma}_u$ across the whole mesh decreases from 29.9μm (a) to 29.3μm (b), and then to 27.5μm (c). Adding a camera to a specific region further reduced local uncertainties [26]. This trend is explained by the fact that the global $[\mathbf{M}_{DIC}]$ matrix is the sum of the contributions from each camera, and the covariance matrix of the measured degrees of freedom is proportional to $[\mathbf{M}_{DIC}]^{-1}$ [51]. Therefore, M-DIC helps to improve the trustworthiness of the measured displacements by decreasing their uncertainties.

$\mathbf{SNR}_u$ was calculated following Eq.(19). The resulting sensitivity fields are shown in Figure 10 for M-DIC configuration. The initial results demonstrate that the variations in the displacement field are concentrated close to the joints, which was expected since only the joint parameters in the model are modified. The non-linear parameters appear to be activated first in the lower part of the joint and then propagate throughout the joint from index 30 onwards, consistent with the force sensitivity observations.

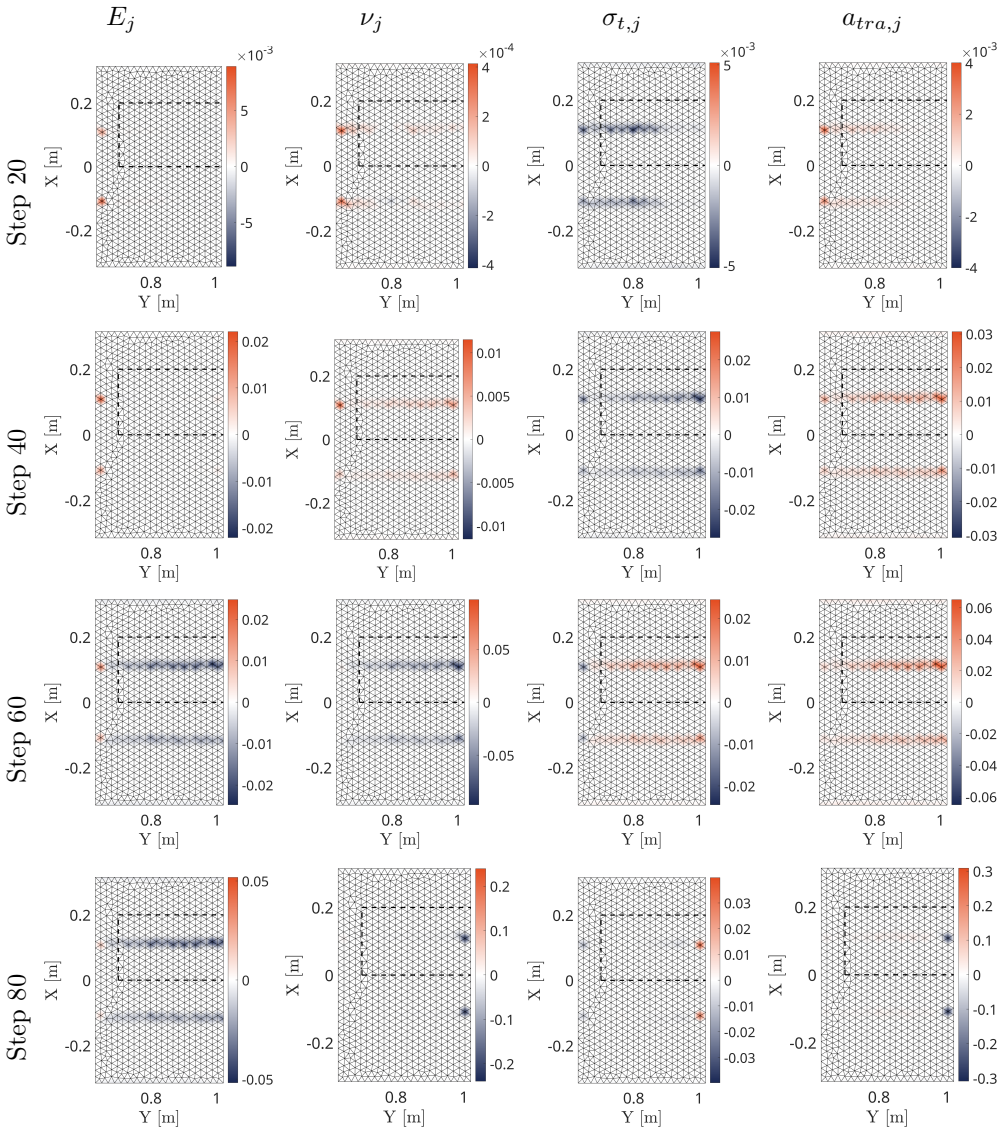

Fig. 10: Sensitivity fields $\mathbf{SNR}_u$ in the X-direction. Each column shows the sensitivity field for the parameters E_j, ν_j, $\sigma_{t,j}$, and $a_{tra,j}$ (from left to right), at different time steps from top to bottom: 20, 40, 60, and 80. The mesh axes have been rotated for better readability, with the y-axis displayed horizontally and the x-axis vertically.

Regarding SNR levels for displacements, they are lower than those observed for force sensitivities at the same time index, with some values falling below 1 for the initial index. This observation suggests that a 1% change in the parameter leads to a variation on the same scale as the measurement noise. This trend could affect the

accuracy of the identification results [31, 52]. In the final steps, the values are higher, and it is noteworthy that increased values occur in the area monitored by Camera 4, which coincides with lower uncertainties $\boldsymbol{\gamma}_u$. The interest of M-DIC in the parameter identification process is confirmed. Similar results are observed for sensitivity fields $\mathbf{SNR}_u$ along the Y-direction. For the Z-direction, since the model is assumed to be planar, the $\mathbf{SNR}_u$ obtained in this direction is zero.

As a preliminary conclusion, considering the force and displacement sensitivities, it is feasible to couple them in the calibration process since they exhibit SNR values greater than 1, making the signals distinguishable from noise. This approach, which incorporates force and M-DIC displacement data, would provide complementary information. Instead of relying on a single force measurement at time t, there would be one force measurement and displacement measurements at each mesh point. While these data points are highly informative, the sensitivities are generally lower. The risk in coupling them lies in the potential degradation of overall calibration accuracy, calling for careful weighting. The following subsection focuses on the minimization problem to be solved to identify the model parameters.

4.3.2 Formulation of the FEMU Problem

The main interest of the approach presented in this paper is the a priori study of the identifiability of the model parameters using classical identification methods, such as Finite Element Model Updating (FEMU). The goal of FEMU is to minimize the difference between the experimental results and those obtained through simulations to adjust the model parameters $\{\mathbf{p}\}$ [53]. This minimization is formulated in terms of a cost function to minimize

$$\min_{\mathbf{p}} \boldsymbol{\chi}^2(\{\mathbf{p}\}) \tag{13}$$

For the triplet shear tests, the force and displacement data acquired using the multi-view system are expected to enable the identification of the model parameters. The cost function $\boldsymbol{\chi}^2(\{\mathbf{p}\})$ is thus defined as a combination of two terms: one comparing the measured and simulated force responses, and the other comparing the measured and simulated displacement fields [54].

$$\begin{aligned}
\boldsymbol{\chi}^2(\{\mathbf{p}\}) &= \boldsymbol{\chi}^2_{\mathbf{F}}(\{\mathbf{p}\}) + \boldsymbol{\chi}^2_{\mathbf{u}}(\{\mathbf{p}\}) \\
\boldsymbol{\chi}^2_{\mathbf{F}}(\{\mathbf{p}\}) &= \frac{1}{N_{t,F}}(\{\mathbf{F}_{exp}\} - \{\mathbf{F}_{sim}\}(\{\mathbf{p}\}))^T \frac{1}{\gamma_F^2}(\{\mathbf{F}_{exp}\} - \{\mathbf{F}_{sim}\}(\{\mathbf{p}\})) \\
\boldsymbol{\chi}^2_{\mathbf{u}}(\{\mathbf{p}\}) &= \frac{1}{N_{dof,u}N_{t,u}} \sum_t \Big(\{\mathbf{u}_{exp}\}_t - \{\mathbf{u}_{sim}\}_t(\{\mathbf{p}\})\Big)^T \\
&\quad \times \frac{[\mathbf{M}_{DIC}]}{2\sigma^2}\Big(\{\mathbf{u}_{exp}\}_t - \{\mathbf{u}_{sim}\}_t(\{\mathbf{p}\})\Big)
\end{aligned} \tag{14}$$

with $N_{t,F}$ representing the number of force data points acquired and used for the minimization in time, $N_{t,u}$ and $N_{dof,u}$ representing the number of displacement data points in time and space, respectively. Both vectors are projected spatially onto the measurement mesh and temporally onto the experimental time basis. Two sensitivity matrices are defined as [55, 56]

$$\begin{aligned}
S_F(t,i) &= \frac{F^{(i)}(t,\{\mathbf{p}^{(i)}\}) - F^{(0)}(t,\{\mathbf{p}^{(0)}\})}{\partial\{\mathbf{p}^{(i)}\}} \\
\{\mathbf{S}_u(t,i)\} &= \frac{\{\mathbf{u}^{(i)}_{FE}(t,\{\mathbf{p}^{(i)}\})\} - \{\mathbf{u}^{(0)}_{FE}(t,\{\mathbf{p}^{(0)}\})\}}{\partial\{\mathbf{p}^{(i)}\}}
\end{aligned} \tag{15}$$

The solution to the FEMU least-squares problem is obtained using a Gauss-Newton method, which yields the parameter increment $\{\delta\mathbf{p}\}$ at each iteration step until convergence is achieved [55, 56]

$$(w_f[\mathbf{H}_F] + w_u[\mathbf{H}_u])\{\delta\mathbf{p}\} = w_f[\mathbf{B}_F] + w_u[\mathbf{B}_u] \tag{16}$$

where w_f and w_u are the weights for force and displacement respectively. Their expressions ensure that both types of measurements contribute equally to the identification

process, accounting for their respective uncertainties and scales

$$
\begin{aligned}
[\mathbf{H}_F] &= [\mathbf{S}_F]^T \frac{1}{\gamma_F^2} [\mathbf{S}_F] \; ; \; w_f = \frac{1}{N_{t,F}} \\
[\mathbf{H}_u] &= [\mathbf{S}_u]^T \frac{[\mathbf{M}_{DIC}]}{2\sigma^2} [\mathbf{S}_u] \; ; \; w_u = \frac{1}{N_{t,u} N_{dof,u}}
\end{aligned} \tag{17}
$$

$$
\begin{aligned}
[\mathbf{B}_F] &= \frac{1}{\gamma_f^2} [\mathbf{S}_F]^T \left(\{\mathbf{F}_{ref}\} - \{\mathbf{F}_{sim}(\{\mathbf{p}\})\} \right) \\
[\mathbf{B}_u] &= \frac{1}{2\sigma^2} [\mathbf{S}_u]^T [\mathbf{M}_{DIC}] \left(\{\mathbf{u}_{ref}\} - \{\mathbf{u}_{sim}(\{\mathbf{p}\})\} \right)
\end{aligned} \tag{18}
$$

Weighted FEMU enables for the integration of heterogeneous data sources, namely, force and displacement measurements into a unique cost function. Since it was chosen to prescribe the same 1% variation on all parameters for the virtual tests, it was decided to normalize the previous expressions by writing for each test i [30]

$$
\begin{aligned}
\delta \hat{\mathbf{p}}_i &= \frac{p_i}{p_{0,i}} \\
[\hat{\mathbf{S}}_F(t,i)] &= \frac{\mathbf{F}^{(i)}(t,\{p_i\}) - \mathbf{F}^{(0)}(t,\{p_0\})}{0.01\gamma_F} \\
[\hat{\mathbf{S}}_u(t,i)] &= \frac{\mathbf{u}^{(i)}(t,\{p_i\}) - \mathbf{u}^{(0)}(t,\{p_0\})}{0.01\sqrt{2}\sigma}
\end{aligned} \tag{19}
$$

Equation (16) becomes

$$
\left(w_f [\hat{\mathbf{H}}_F] + w_u [\hat{\mathbf{H}}_u] \right) \{\delta \hat{\mathbf{p}}\} = w_f [\hat{\mathbf{B}}_F] + w_u [\hat{\mathbf{B}}_u] \tag{20}
$$

with [31]

$$
\begin{aligned}
[\hat{\mathbf{H}}_F] &= [\hat{\mathbf{S}}_F]^T [\hat{\mathbf{S}}_F] \\
[\hat{\mathbf{H}}_u] &= [\hat{\mathbf{S}}_u]^T [\mathbf{M}_{DIC}] [\hat{\mathbf{S}}_u]
\end{aligned} \tag{21}
$$

From Equation (20), it follows that the sensitivity of the parameters can be assessed by analyzing the global Hessian matrix $\left(w_f [\hat{\mathbf{H}}_F] + w_u [\hat{\mathbf{H}}_u] \right)$. The following section presents a detailed analysis of force-based and displacement-based Hessian matrices to assess their respective sensitivities and determine whether both data types need to be accounted for in the identification process.

4.3.3 Hessian Matrix analysis

Virtual testing allows for the *a priori* determination of the DIC Hessian matrix $[\mathbf{M}_{DIC}]$, providing a more detailed understanding of $[\hat{\mathbf{H}}_u]$ compared to traditional sensitivity analysis, which would only use $[\hat{\mathbf{S}}_u]$. Specifically, Figure 11 presents the eigenvalues of $[\mathbf{M}_{DIC}]$ for four different camera configurations. In the monoview setup

(Camera 1), the matrix exhibits the lowest eigenvalues and poor conditioning, likely due to difficulty determining displacements along the z-axis. Adding a new camera (Cameras 1+4) significantly increases the eigenvalues for modes corresponding to the nodes in the zoomed area but does not improve the final conditioning. In contrast, the 3D-DIC (Cameras 2+3) and M-DIC (Cameras 1+2+3+4) configurations show better conditioning, even with noisy reference images, highlighting good stability. The M-DIC configuration achieves the highest eigenvalues for all modes.

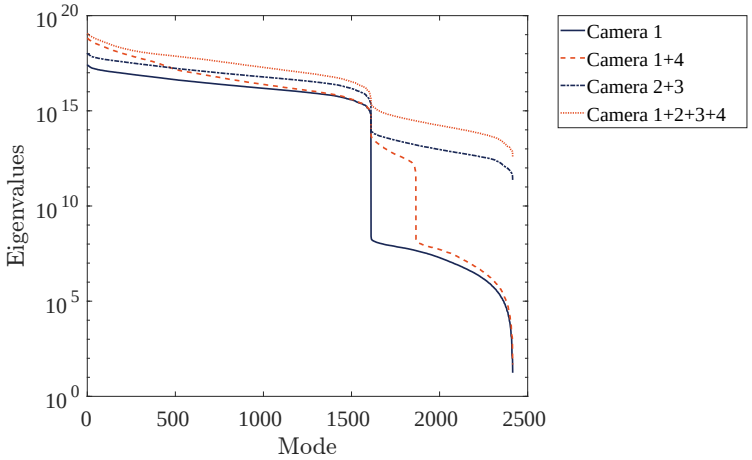

Fig. 11: Eigenvalues of $[\mathbf{M}_{DIC}]$ for different camera configurations

The static Hessian matrix $[\hat{\mathbf{H}}_F]$ is presented in Figure 12a, with absolute values shown in decimal logarithms, along with their respective eigen decomposition, sorted in descending order of eigenvalue magnitude. This matrix shows strong sensitivity to all the parameters, with a relatively low condition number, close to 1.25, indicating a very stable identification of the parameters. The analysis of the eigenvectors reveals many correlations between parameters but suggests that it will be relatively easy to identify each parameter individually (as seen in eigenvectors 2 to 6, where one parameter stands out significantly). However, c_{fj} remains an exception, as it is strongly correlated with all the other parameters.

The same analysis is applied to the Hessian matrix related to displacement measurements, focusing on the M-DIC configuration (Cameras 1+2+3+4) (Figure 12b). It is interesting to observe different correlations between parameters, with each eigenparameter predominantly activating one original parameter. However, the eigenvalues are significantly lower— at least 12 orders of magnitude smaller compared to the static Hessian matrix - and negative. Additionally, it is noted that the conditioning is now higher, equal to 5.19. These results suggest higher uncertainties and less stable identification in the identification process. Consequently, greater emphasis should be placed on the force data.

In order to validate the use of M-DIC for parameter identification, the previous Hessian matrix can be compared with the one obtained after processing the measurements from Cameras 2+3 (Figure 12c). It is notable that the correlations between the parameters appear to be similar, but the eigenvalues are approximately half an order of magnitude higher in the M-DIC configuration.

Moreover, considering the sensitivities to forces and displacements, the virtual tests suggest that if both were coupled in the cost function, the calibration would primarily be driven by the force data (Figure 12d). One possible expression for the global Hessian matrix reads

$$[\hat{\mathbf{H}}] = w_f[\hat{\mathbf{H}}_F] + w_u[\hat{\mathbf{H}}_u] \tag{22}$$

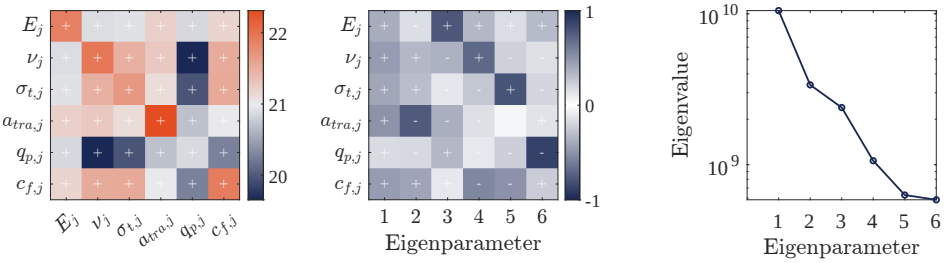

(a) Normalized Hessian matrix $[\hat{\mathbf{H}}_F]$ in decimal logarithm, associated with force **F** measurements (left), along with its eigen decomposition (middle) and eigenvalues (right).

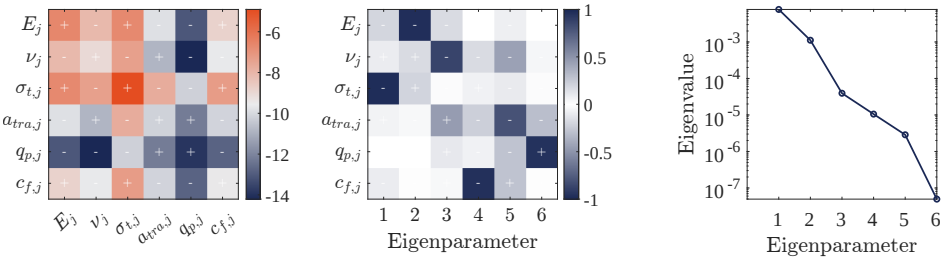

(b) Normalized Hessian matrix $[\hat{\mathbf{H}}_u]$ in decimal logarithm, associated with displacement **u** measurements for Cameras 1+2+3+4 (left), along with its eigen decomposition (middle) and eigenvalues (right).

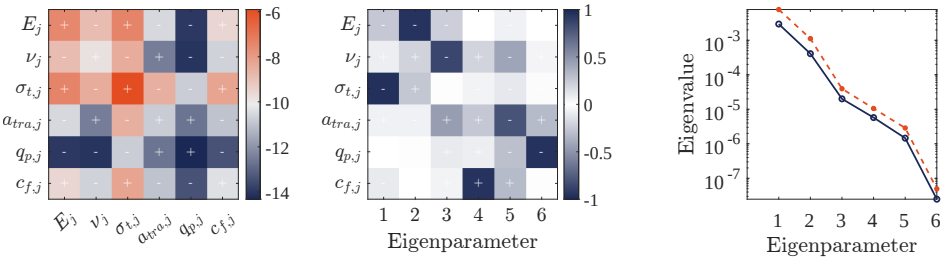

(c) Normalized Hessian matrix $[\hat{\mathbf{H}}_u]$ in decimal logarithm, associated with **u** measurements for Cameras 2+3 (left), along with its eigen decomposition (middle) and eigenvalues (right). The values in orange represent the eigenvalues in the MDIC configuration.

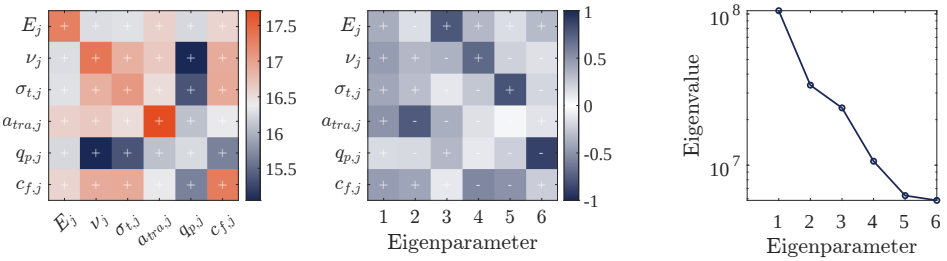

(d) Normalized Hessian matrix $[\hat{\mathbf{H}}]$ in decimal logarithm for Cameras 1+2+3+4 (left), along with its eigen decomposition (middle) and eigenvalues (right).

Fig. 12: Comparison of normalized Hessian matrices and their eigen decompositions for different data types and DIC configurations.

In this scenario, all parameters can be identified essentially based on force measurements, which was the goal of the virtual design phase. Otherwise, one could have adjusted the testing approach to activate all the parameters. Multi-view image correlation enhances the likelihood of accurately identifying parameters within a specific region, even though the orders of magnitude remain lower than those observed for a force-based Hessian matrix [31]. However, in the case of this study, M-DIC would not be suitable to identify the model parameters. Nevertheless, the proposed approach could be applicable when force and displacement data are combined within the FEMU framework.

4.4 Uncertainty quantification

Another key aspect of this study is the *a priori* estimation of the uncertainties associated with each parameter through FEMU. Since this method relies on displacement measurements obtained via DIC, it inherently accounts for all uncertainties within the measurement chain. By minimizing these uncertainties, the analysis subsequently guides the optimization of experimental parameters such as the speckle size. Equation (16) reads

$$\{\delta\mathbf{p}\} = [\mathbf{H}_u]^{-1}[\mathbf{B}_u]^T\{\delta\mathbf{u}\} \tag{23}$$

$$= \left([\mathbf{S}_u]^T[\mathbf{M}_{DIC}][\mathbf{S}_u]\right)^{-1}[\mathbf{S}_u]^T[\mathbf{M}_{DIC}]\{\delta\mathbf{u}\} \tag{24}$$

The covariance matrix of the displacement field, when noise is the primary source of variability, is proportional to the inverse of the global DIC matrix $[\mathbf{M}_{DIC}]$ [33, 57–59]

$$[\mathbf{C}_u] \equiv \langle\{\delta\mathbf{u}\} \otimes \{\delta\mathbf{u}\}\rangle = 2\sigma^2[\mathbf{M}_{DIC}]^{-1} \tag{25}$$

with σ^2 defined as the variance of image acquisition noise (assumed to be Gaussian and uncorrelated at the pixel scale). This value has been set in Blender as $\sigma^2 = 2$ gray levels. Similarly, the covariance matrix of the parameters to be identified is proportional to the inverse of the Hessian matrix $\left([\mathbf{S}_u]^T[\mathbf{M}_{DIC}][\mathbf{S}_u]\right)$ [55]

$$[\mathbf{C}_p] \equiv \langle\{\delta\mathbf{p}\} \otimes \{\delta\mathbf{p}\}\rangle = 2\sigma^2\left([\mathbf{S}_u]^T[\mathbf{M}_{DIC}][\mathbf{S}_u]\right)^{-1} \tag{26}$$

where the diagonal terms provide the variance for each parameter individually, with all other parameters held at their nominal values. The covariance matrix enables for a comprehensive analysis of the overall uncertainty by considering the interactions between all parameters [55]. The matrix $[\mathbf{V}]$ of eigenvectors and the diagonal matrix $[\mathbf{D}]$ of eigenvalues are introduced

$$[\mathbf{S}_u]^T[\mathbf{M}_{DIC}][\mathbf{S}_u] = [\mathbf{V}]^T[\mathbf{D}][\mathbf{V}] \tag{27}$$

The variance of the parameter p_k is defined by [55]

$$\sigma_{p_k}^2 = 2\sigma^2 \sum_i \frac{V_{k,i}^2}{D_{i,i}} \tag{28}$$

This equation considers the fluctuations of all parameters, unlike simply selecting the diagonal elements of $\left([\mathbf{S}_u]^T[\mathbf{M}_{DIC}][\mathbf{S}_u]\right)^{-1}$, which assumes they are uncorrelated [55]. The results for both 3D-DIC (Cameras 2+3) and M-DIC displacement measurements are presented in Table 6. The use of the M-DIC configuration helps reduce uncertainties in the identification of the model parameters. The variance for each parameter is not acceptable, which is consistent with the negative eigenvalues of $[\hat{\mathbf{H}}_u]$. The lowest value corresponds to the parameter identifiable by the eigenvector associated with the smallest eigenvalue (Figure 12b). In the case of a test with greater sensitivity to displacement fields, this approach ensures that each parameter will be identifiable in the final analysis. This method is used to optimize the speckle pattern but could be applied to optimizing any experimental parameter that impacts the measurement chain.

Table 6: Uncertainty quantifications for displacement measurements

Parameter	E_j	ν_j	$\sigma_{t,j}$	$a_{tra,j}$	$q_{p,j}$	$c_{f,j}$
Unit	Pa	/	Pa	$\mathrm{kJ}^{-1} \cdot \mathrm{m}^3$	/	/
Value	22×10^9	0.19	8.4×10^5	4×10^{-3}	6.5	2.89
σ_p (3D-DIC)	1.4×10^{12}	68	8.7×10^7	5.7×10^3	2.7×10^4	9.3×10^2
σ_p (M-DIC)	1.0×10^{12}	49	6.0×10^7	4.1×10^3	2.0×10^4	6.9×10^2
σ_p ($d = 5$mm)	9.8×10^{11}	46	5.6×10^7	3.8×10^3	1.8×10^4	6.4×10^2
σ_p ($d = 2.5$mm)	8.4×10^{11}	40	4.9×10^7	3.3×10^3	1.6×10^4	5.6×10^2

4.5 Speckle Optimization

Bossuyt [60] proposed theoretical insights into creating an optimal speckle pattern. The present approach differs slightly. Its novelty lies in leveraging Blender and BlenDIC to determine a speckle pattern that reduces uncertainties in parameter identification. This point is particularly interesting for specimens where the speckle pattern can be directly printed. In the present case, perforated grids were selected with "dots" of a particular diameter d. Thus, one is interested in finding the value of d that minimizes the measurement uncertainties. A basic script is used to generate realistic speckle patterns in Blender. The pattern is slightly randomized regarding circle positions and black intensity to simulate the variability observed when spraying black paint onto the specimen through grids. They are then mapped onto the specimen surface (Figure 13).

At this step, it is not necessary to rerun the FE simulations, as the speckle pattern only affects the Hessian matrix $[\mathbf{M}_{DIC}]$. Therefore, it is sufficient to recalculate the expressions for the kinematic Hessian matrices for each type of speckle pattern and derive the associated parameter uncertainties.

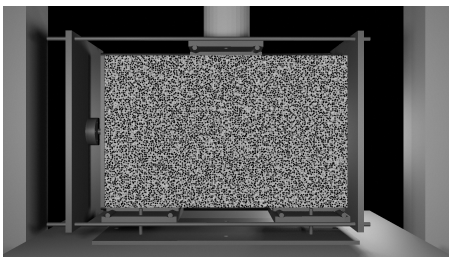

(a) $d = 2.5$mm (Camera 1)

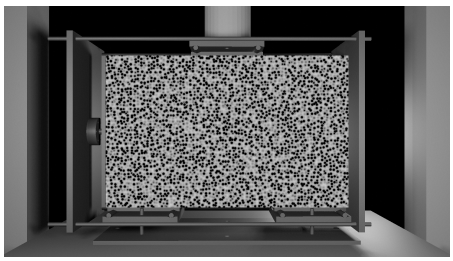

(b) $d = 5$mm (Camera 1)

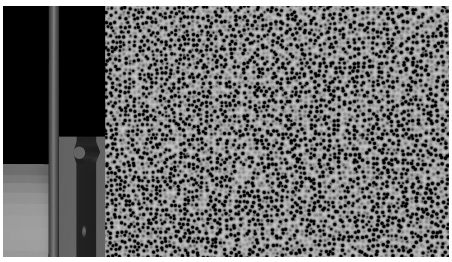

(c) $d = 2.5$mm (Camera 4)

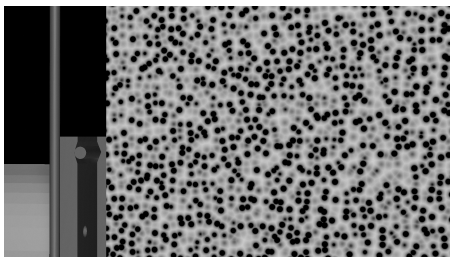

(d) $d = 5$mm (Camera 4)

Fig. 13: Virtual images generated by BlenDIC with different sizes of speckle patterns for two cameras. (a)-(b) correspond to Camera 1, and (c)-(d) to Camera 4.

By comparing the results for two speckle patterns with sizes 5 mm and 2.5 mm, it is observed that the finer the speckle pattern, the more the measurement uncertainties decrease. A coarse speckle pattern fails to capture finer phenomena. The measurement uncertainties are reduced by approximately 15% between the two speckle sizes (Table 6).

The focus shifts to even finer speckle patterns ($d = 1.25$ mm or 0.5 mm) to investigate whether the reduction in uncertainties follows a monotonic trend. Figure 14 shows the change of the normalized variance of each parameter relative to the lowest obtained variance. It is observed that the lowest variance for each parameter is obtained for the same diameter ($d = 2.5$ mm). For patterns finer than this value, the measurement uncertainty increases as the value of d decreases. This result suggests that there is an optimal speckle size, estimated to be $d = 2.5$ mm, that minimizes the uncertainties of the parameters identified using displacement measurements.

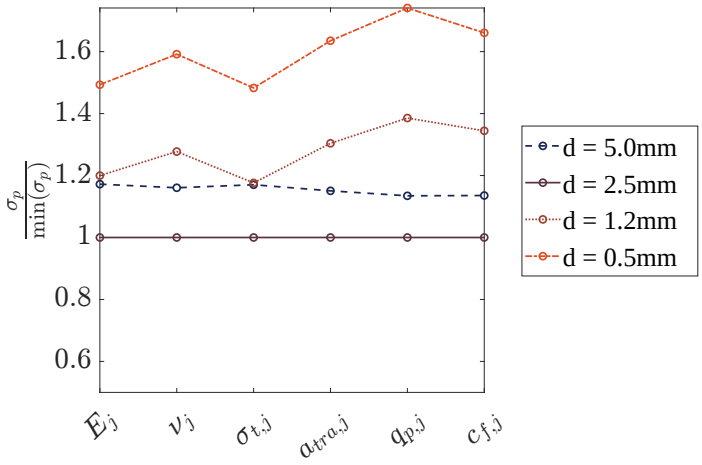

Fig. 14: Evolution of the standard uncertainties σ_p for displacement measurements as functions of speckle size

5 Conclusion

This study explored the potential of digital image correlation (DIC) in designing experiments that may be complex due to factors such as the setup or the number of cameras. A key strength of the proposed approach is that it is not dependent on the specific test conducted. As such, it can be applied to the design of any experiment involving image correlation, particularly those requiring preliminary studies for parameter identification.

Starting from a robust numerical model, which may differ from the one presented in this study, the Design of Experiment (DOE) phase helps to better understand the sensitivities to geometric parameters and select the combination most likely to produce insightful results. The virtual design phase preceding the experiments enables a good configuration of all elements in the virtual setup. In particular, for the cameras, each one is positioned in space, as well as lighting. The ability to generate virtual and realistic images using Blender made it possible to quantify measurement uncertainties by accounting for the entire measurement chain.

The results highlighted the value of a multiscale and multiview system for reducing displacement uncertainties in the region of interest monitored by the near-field camera, particularly in this study, at the mortar joint where cracking is expected. Although this approach requires a more complex experimental setup with a larger number of cameras, virtual modelling of the experimental system enables the optimization of camera placement and significantly reduces setup time.

The virtual tests combined with a comprehensive sensitivity analysis ensure that the model parameters can be identified by coupling force and displacement measurements. The results indicated a stronger sensitivity to force measurements in the present case. However, the use of a multiview system enhanced parameter sensitivity in the region of interest captured by the near-field camera and contributed to reduced

uncertainties associated with each identified parameter. The influence of the speckle pattern on the uncertainties in parameter identification was also demonstrated, along with the ability to virtually test multiple patterns in order to select the one that minimizes the uncertainties. This optimal pattern may be printed or directly applied to the specimen.

The success of the virtual design phase relies on selecting a model trustworthy enough to replicate the expected behavior across different tests. Further research is needed to compare the outcomes of the virtual testing strategy with those obtained from a conventional experimental campaign to validate the overall approach. Future work will also extend these findings by fully implementing the FEMU algorithm to test convergence from different initial parameter sets to a unique — or not — final set.

Acknowledgements. The ERMES Department of EDF R&D and the École Normale Supérieure Paris Saclay (ENS Paris Saclay) are kindly thanked for financial supports. The research reported in this paper has been supported in part by the SEISM Paris Saclay Research Institute. Thanks are extended to Guillaume Hervé-Secourgeon for his valuable support.

Author contributions. All authors contributed to the study design. Material preparation, data collection and analysis were performed by LC. The first draft of the manuscript was written by LC and all authors commented on previous versions of the manuscript. All authors read and approved the final manuscript.

Declarations

- Conflict of interest: The authors declare that they have no known competing financial interests or personal relationships that could have appeared to influence the work reported in this paper.

Appendix A Concyc Law

The mechanical behavior of the material is separated into contributions from the matrix (modeled as a continuum medium with damage) and the crack, represented as [43, 44]

$$\boldsymbol{\sigma} = \boldsymbol{\sigma}^m + \boldsymbol{\sigma}^f \tag{A1}$$

For the continuum medium, an isotropic damage model is applied to describe the behavior of the matrix

$$\boldsymbol{\sigma}^m = (1 - D)\mathbf{C} : \boldsymbol{\epsilon} \tag{A2}$$

where D is the damage scalar, $\mathbf{C}$ the Hooke tensor, and $\boldsymbol{\epsilon}$ the strain tensor. The evolution of damage follows a Mazars-like failure criterion

$$D = 1 - \frac{Y_0}{\bar{Y}} \exp\left(-\frac{a_{\mathrm{tra},j}}{\kappa}(\bar{Y} - Y_0)\right) \tag{A3}$$

$$\tag{A4}$$

where $\bar{Y}(\sigma_{t,j})$ is the equivalent strain energy release rate, $Y_0(\sigma_{t,j})$ is the initial damage threshold, and κ is the parameter introduced to take into account the confining pressure. For the cracks, the following assumption is made regarding the evolution of $\boldsymbol{\sigma}^f$

$$\dot{\boldsymbol{\sigma}}^f = \vartheta(\boldsymbol{\epsilon}^f, q_{p,j})\mathbf{C} : \dot{\boldsymbol{\epsilon}}^f \tag{A5}$$

$$\vartheta = 1 - \frac{1}{1 + \exp\left(-q_{p,j}\frac{\mathbf{I_1}(\boldsymbol{\epsilon}^f)}{\mathbf{I_1}(\boldsymbol{\epsilon}^f_{\max})}\right)} \tag{A6}$$

where $\vartheta(\boldsymbol{\epsilon}^f, q_{p,j})$ is a scalar depending on parameter $q_{p,j}$. To model the frictional sliding occurring at the crack surfaces, a perfect plasticity model with a Drucker–Prager criterion is employed

$$\varphi^f = \sqrt{J_2\left(\boldsymbol{\sigma}^f\right)} + c_{f,j} I_1\left(\boldsymbol{\sigma}^f\right) \tag{A7}$$

Appendix B Parametric analysis for designing the specimen geometry

Figures B1a, B1b, B1c shows the results of the virtual tests that determined the effect of each geometric parameter on the force-displacement curve. Figure B1d displays the results of the four Taguchi test case simulations.

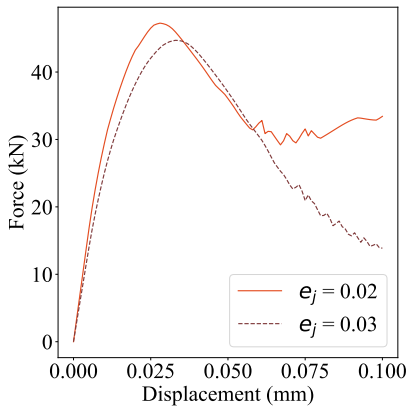

(a) Influence of the joint thickness.

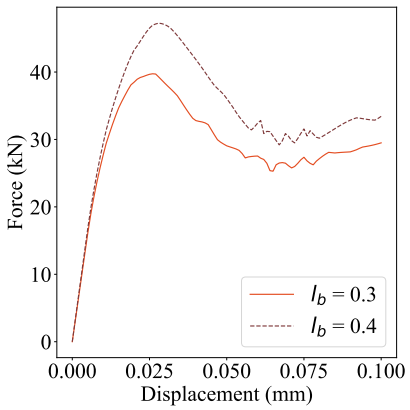

(b) Influence of the block length.

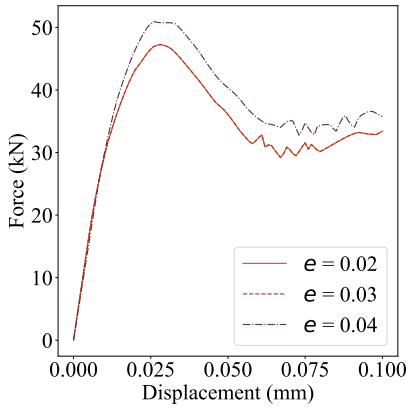

(c) Influence of the support positions.

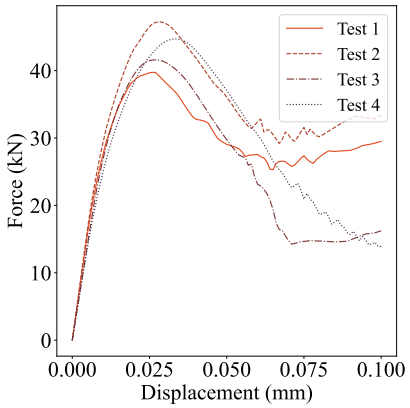

(d) Taguchi test cases.

Fig. B1: Evolution of the force-displacement curve for different joint thicknesses (a), block lengths (b), and support positions (c). Force-displacement curves for Taguchi test cases (d).

Appendix C Parametric analysis for FEMU application

Table C1 shows the coefficient values required for each numerical simulation to perform a sensitivity analysis for the FEMU application. Starting with an initial set of parameters $\{\mathbf{p}_0\}$ (Test 0), additional simulations are conducted by increasing each parameter value by 1% to determine its impact.

Table C1: Set of parameters for virtual test campaign

Parameter	E_j	ν_j	$\sigma_{t,j}$	$a_{tra,j}$	$q_{p,j}$	$c_{f,j}$
Unit	Pa	/	Pa	$\mathrm{kJ}^{-1} \cdot \mathrm{m}^3$	/	/
Value	22×10^9	0.19	8.4×10^5	4×10^{-3}	6.5	2.89
Test 0	1	1	1	1	1	1
Test 1	1.01	1	1	1	1	1
Test 2	1	1.01	1	1	1	1
Test 3	1	1	1.01	1	1	1
Test 4	1	1	1	1.01	1	1
Test 5	1	1	1	1	1.01	1
Test 6	1	1	1	1	1	1.01

For each simulation, the obtained force-displacement curve is compared to the reference curve (Test 0). The results are displayed in Figure C2.

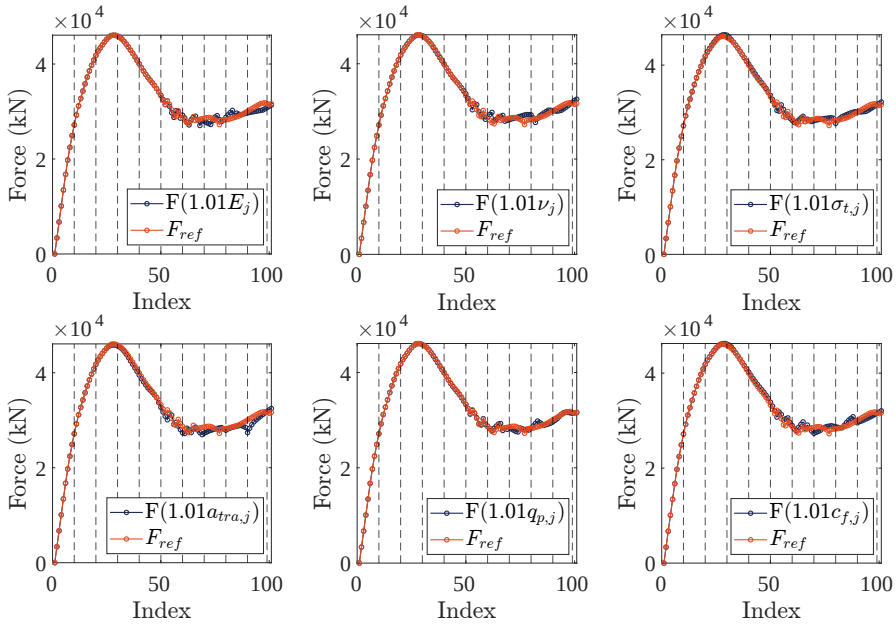

Fig. C2: Comparison between the reference force-displacement curve and the curve where the mentioned parameter has increased by 1%.

Appendix D DIC application

The parameters of the M-DIC calculation are summarised in Table D2.

Table D2: DIC parameters for the virtual shear test

Parameter	M-DIC Configuration
DIC software	Correli 3.0 [50]
Image filtering	None
Element sizes	20 mm
Shape functions	Linear (T3 elements)
Matching criterion	Sum of squared differences
Interpolant	Spline

The generation of noisy virtual images enables the quantification of measurement uncertainties across different camera configurations. The results are presented in Figure D3. Notably, the M-DIC configuration leads to a reduction in uncertainties within the region where camera 4 provides a zoomed view.

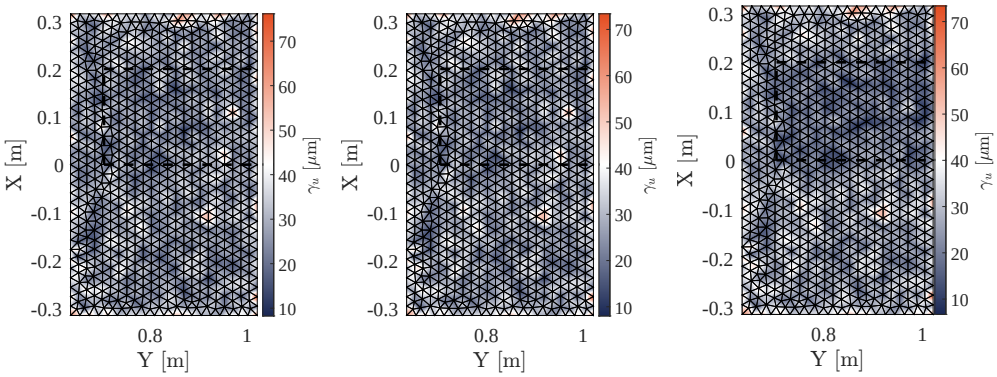

(a) Cameras 2+3 (b) Cameras 1+2+3 (c) Cameras 1+2+3+4

Fig. D3: Standard displacement uncertainty fields (in μm) associated with various camera configurations. The dashed rectangle indicates the region of interest of Camera 4.

References

[1] M. Dhanasekar, A.W. Page, P.W. Kleeman, The failure of brick masonry under biaxial stresses. Proceedings of the Institution of Civil Engineers **79**(2), 295–313 (1985)

[2] D. Dais, I.E. Bal, E. Smyrou, V. Sarhosis, Automatic crack classification and segmentation on masonry surfaces using convolutional neural networks and transfer learning. Automation in Construction **125**, 103606 (2021). https://doi.org/10.1016/j.autcon.2021.103606

[3] J.A. Thamboo, M. Dhanasekar, C. Yan, Flexural and shear bond characteristics of thin layer polymer cement mortared concrete masonry. Construction and Building Materials **46**, 104–113 (2013)

[4] G. Andreotti, F. Graziotti, G. Magenes, Detailed micro-modelling of the direct shear tests of brick masonry specimens: the role of dilatancy. Engineering Structures **168**, 929–949 (2018)

[5] D.V. Bompa, A.Y. Elghazouli, Experimental and numerical assessment of the shear behaviour of lime mortar clay brick masonry triplets. Construction and Building Materials **262**, 120571 (2020). https://doi.org/10.1016/j.conbuildmat.2020.120571

[6] S. Barattucci, V. Sarhosis, A.W. Bruno, A.M. D'Altri, S. de Miranda, G. Castellazzi, An experimental and numerical study on masonry triplets subjected to monotonic and cyclic shear loadings. Construction and Building Materials **254**, 119313 (2020). https://doi.org/10.1016/j.conbuildmat.2020.119313

[7] P.K. Dhir, E. Tubaldi, A. Orfeo, H. Ahmadi, Cyclic shear behaviour of masonry triplets with rubber joints. Construction and Building Materials **351**, 128356 (2022). https://doi.org/10.1016/j.conbuildmat.2022.128356

[8] S. Calderón, C. Sandoval, G. Araya-Letelier, V. Aguilar, A detailed experimental mechanical characterization of multi-perforated clay brick masonry. Journal of Building Engineering **63**, 105505 (2023)

[9] F. Stazi, M. Serpilli, G. Chiappini, M. Pergolini, E. Fratalocchi, S. Lenci, Experimental study of the mechanical behaviour of a new extruded earth block masonry. Construction and Building Materials **244**, 118368 (2020). https://doi.org/10.1016/j.conbuildmat.2020.118368

[10] L. Garcia-Ramonda, L. Pelà, P. Roca, G. Camata, Experimental and numerical insights on the in-plane behaviour of unreinforced and trm/srg retrofitted brick masonry walls by diagonal compression and shear-compression testing. Construction and Building Materials **402**, 132997 (2023). https://doi.org/10.1016/j.conbuildmat.2023.132997

[11] N. Guerrero, M. Martinez, R. Picón, M.E. Marante, F. Hild, S. Roux, J. Flórez-López, Experimental analysis of masonry infilled frames using digital image correlation. Materials and Structures **47**(5), 873–884 (2014). https://doi.org/10.1617/s11527-014-0330-6

[12] R. Ghorbani, F. Matta, M.A. Sutton, Full-field deformation measurement and crack mapping on confined masonry walls using digital image correlation. Experimental Mechanics **55**, 227–243 (2015)

[13] V.F. Sciuti, R. Vargas, N. Guerrero, M.E. Marante, F. Hild, Digital image correlation analyses of masonry infilled frame: Uncertainty-based mesh refinement and damage quantification. Mathematics and Mechanics of Solids (2023)

[14] C. Allen, M.J. Masia, A.W. Page, M.C. Griffith, H. Derakhshan, N. Mojsilovic, *Experimental testing of unreinforced masonry walls with openings subject to cyclic in-plane shear*, in *Proc., 16th Int. Brick & Block Masonry Conf. (IBMAC)* (CRC Press, 2016)

[15] P.A. Korswagen, M. Longo, E. Meulman, J.G. Rots, Crack initiation and propagation in unreinforced masonry specimens subjected to repeated in-plane loading during light damage. Bulletin of Earthquake Engineering **17**, 4651–4687 (2019)

[16] European Committee for Standardization, En 1052-3: 2002; methods of test for masonry—part 3: Determination of initial shear strength. Brussels, Belgium (2002)

[17] S. Petry, K. Beyer, Cyclic test data of six unreinforced masonry walls with different boundary conditions. Earthquake Spectra **31**(4), 2459–2484 (2015)

[18] D. Raffard, P. Ienny, J.P. Henry, Displacement and strain fields at a stone/mortar interface by digital image processing. Journal of Testing and Evaluation **29**(2), 115–122 (2001)

[19] M.H. Shih, S.H. Tung, J.C. Kuo, W.P. Sung, *The application of a digital image correlation method for crack observation*, in *8th International Conference on Computational Structures Technology (CST 2006)* (Civil-Comp Press, 2006)

[20] J. Réthoré, F. Hild, S. Roux, Shear-band capturing using a multiscale extended digital image correlation technique. Computer Methods in Applied Mechanics and Engineering **196**(49-52), 5016–5030 (2007)

[21] M. Bolhassani, A. Hamid, S. Rajaram, P. Vanniamparambil, I. Bartoli, A. Kontsos, Failure analysis and damage detection of partially grouted masonry walls by enhancing deformation measurement using dic. Engineering structures **134**, 262–275 (2017)

[22] L. Binda, M. Facchini, G.M. Roberti, C. Tiraboschi, Electronic speckle interferometry for the deformation measurement in masonry testing. Construction and building materials **12**(5), 269–281 (1998)

[23] G. Livitsanos, N. Shetty, E. Verstrynge, M. Wevers, D. Van Hemelrijck, D. Aggelis, Shear failure characterization in masonry components made with different

mortars based on combined ndt methods. Construction and Building Materials **220**, 690–700 (2019)

[24] S. Peng, T. Parent, Z.M. Sbartaï, S. Morel, Damage monitoring of masonry structures using the acoustic emission technique–from tensile and shear characterization tests to shear wall tests. Engineering Fracture Mechanics **296**, 109845 (2024)

[25] R. Fedele, L. Galantucci, A. Ciani, Global 2d digital image correlation for motion estimation in a finite element framework: a variational formulation and a regularized, pyramidal, multi-grid implementation. International Journal for Numerical Methods in Engineering **96**(12), 739–762 (2013)

[26] I. Hamadouche, D. Seyedi, F. Hild, Damage detection and quantification via multiview dic at varying scales. Experimental Mechanics **64**(5), 675–689 (2024)

[27] K.T. Kavanagh, R.W. Clough, Finite element applications in the characterization of elastic solids. International Journal of Solids and Structures **7**(1), 11–23 (1971)

[28] J.D. Collins, G.C. Hart, T. Hasselman, B. Kennedy, Statistical identification of structures. AIAA journal **12**(2), 185–190 (1974)

[29] H. Leclerc, J.N. Périé, S. Roux, F. Hild, *Integrated digital image correlation for the identification of mechanical properties*, in *Computer Vision/Computer Graphics CollaborationTechniques: 4th International Conference, MIRAGE 2009, Rocquencourt, France, May 4-6, 2009. Proceedings 4* (Springer, 2009), pp. 161–171

[30] L. Turpin, Etude par une approche expérimentale in situ de l'endommagement d'un composite à matrice céramique sous sollicitations multiaxiales. Theses, Université de Bordeaux (2021). URL https://theses.hal.science/tel-03336176

[31] R. Vargas, R. Canto, B. Smaniotto, F. Hild, Calibration of cohesive parameters for a castable refractory using 4d tomographic data and realistic crack path from in-situ wedge splitting test. Journal of the European Ceramic Society **43**(2), 676–691 (2023)

[32] M. Bornert, F. Brémand, P. Doumalin, J.C. Dupré, M. Fazzini, M. Grediac, F. Hild, S. Mistou, J. Molimard, J.J. Orteu, et al., Assessment of digital image correlation measurement errors: methodology and results. Experimental mechanics **49**, 353–370 (2009)

[33] S. Roux, F. Hild, Optimal procedure for the identification of constitutive parameters from experimentally measured displacement fields. International Journal of Solids and Structures **184**, 14–23 (2020)

[34] L. Collin, F. Gatuingt, C. Giry, G. Hervé-Secourgeon, Establishing a test-calculation dialogue for shear tests on masonry triplets. Academic Journal of Civil Engineering **42**(1), 426–436 (2024). https://doi.org/10.26168/ajce.42.1.38. URL https://journal.augc.asso.fr/index.php/ajce/article/view/4745

[35] C. Rouzaud, F. Gatuingt, G. Hervé, N. Moussallam, O. Dorival, Influence of the aircraft crash induced local nonlinearities on the overall dynamic response of a rc structure through a parametric study. Nuclear Engineering and Design **298**, 168–182 (2016)

[36] G. Taguchi, Introduction to quality engineering: designing quality into products and processes. Asian Productivity Organization (1986)

[37] M. Vitse, M. Poncelet, A.E. Iskef, J.E. Dufour, R. Gras, A. Bouterf, B. Raka, C. Giry, F. Gatuingt, F. Hild, et al., Toward virtual design and optimization of a structural test monitored by a multi-view system. The Journal of Strain Analysis for Engineering Design **56**(2), 112–128 (2021)

[38] X. Chang, C. Le Gourriérec, F. Hild, S. Roux, Brightness and contrast corrections for stereocorrelation: Global and instantaneous formulation with spatial regularization. Mechanical Systems and Signal Processing **208**, 111057 (2024). https://doi.org/https://doi.org/10.1016/j.ymssp.2023.111057. URL https://www.sciencedirect.com/science/article/pii/S0888327023009652

[39] M. Razafimbelo, Etude experimentale de la methode des bielles-tirants sur des zones massives en beton arme par l'analyse de deformation pour des chargements complexes. Ph.D. thesis, Universite Paris-Saclay (2022)

[40] B. Ghiassi, G. Milani, *Numerical modeling of masonry and historical structures: from theory to application* (Woodhead Publishing, 2019)

[41] P.K. Dhir, E. Tubaldi, H. Ahmadi, J. Gough, Numerical modelling of reinforced concrete frames with masonry infills and rubber joints. Engineering Structures **246**, 112833 (2021)

[42] I. Boem, B. Patzák, A. Kohoutková, Numerical simulations of masonry elements strengthened through fibre-reinforced mortar: detailed level modelling using the oofem code. Key Engineering Materials **916**, 222–229 (2022)

[43] M. Vassaux, Comportement mécanique des matériaux quasi-fragiles sous sollicitations cycliques: de l'expérimentation numérique au calcul de structures. Ph.D. thesis, École normale supérieure de Cachan-ENS Cachan (2015)

[44] M. Vassaux, B. Richard, F. Ragueneau, A. Millard, Regularised crack behaviour effects on continuum modelling of quasi-brittle materials under cyclic loading. Engineering Fracture Mechanics **149**, 18–36 (2015)

[45] E. de Rocquigny, N. Devictor, S. Tarantola, *Uncertainty in industrial practice: a guide to quantitative uncertainty management* (John Wiley & Sons, 2008)

[46] M. Grédiac, F. Hild, *Full-field measurements and identification in solid mechanics* (John Wiley & Sons, 2012)

[47] J.C. Passieux, F. Bugarin, C. David, J.N. Périé, L. Robert, Multiscale displacement field measurement using digital image correlation: Application to the identification of elastic properties. Experimental Mechanics **55**, 121–137 (2015)

[48] J.E. Dufour, F. Hild, S. Roux, Shape, displacement and mechanical properties from isogeometric multiview stereocorrelation. The Journal of Strain Analysis for Engineering Design **50**(7), 470–487 (2015). https://doi.org/10.1177/0309324715592530. URL https://doi.org/10.1177/0309324715592530

[49] H. Leclerc, J.N. Périé, F. Hild, S. Roux, Digital volume correlation: what are the limits to the spatial resolution? Mechanics & Industry **13**(6), 361–371 (2012)

[50] H. Leclerc, J. Neggers, F. Mathieu, F. Hild, S. Roux, Correli 3.0. Iddn. fr **1**(000) (2015)

[51] M. Berny, T. Archer, P. Beauchêne, A. Mavel, F. Hild, Displacement uncertainty quantifications in t3-stereocorrelation. Experimental Mechanics **61**, 771–790 (2021)

[52] A.P. Ruybalid, J.P. Hoefnagels, O. van der Sluis, M.G. Geers, Comparison of the identification performance of conventional fem updating and integrated dic. International Journal for Numerical Methods in Engineering **106**(4), 298–320 (2016)

[53] E. Pagnacco, A.S. Caro-Bretelle, P. Ienny, Parameter identification from mechanical field measurements using finite element model updating strategies. Full-Field Measurements and Identification in Solid Mechanics pp. 247–274 (2013)

[54] A. Guery, F. Hild, F. Latourte, S. Roux, Identification of crystal plasticity parameters using dic measurements and weighted femu. Mechanics of Materials **100**, 55–71 (2016)

[55] R. Gras, H. Leclerc, F. Hild, S. Roux, J. Schneider, Identification of a set of macroscopic elastic parameters in a 3d woven composite: Uncertainty analysis and regularization. International Journal of Solids and Structures **55**, 2–16 (2015)

[56] T. Archer, M. Berny, P. Beauchêne, F. Hild, Creep behavior identification of an environmental barrier coating using full-field measurements. Journal of the European Ceramic Society **40**(15), 5704–5718 (2020)

[57] F. Hild, S. Roux, Digital image correlation: from displacement measurement to identification of elastic properties–a review. Strain **42**(2), 69–80 (2006)

[58] J. Réthoré, A fully integrated noise robust strategy for the identification of constitutive laws from digital images. International Journal for Numerical Methods in Engineering **84**(6), 631–660 (2010)

[59] H. Leclerc, J.N. Périé, S. Roux, F. Hild, Voxel-scale digital volume correlation. Experimental mechanics **51**, 479–490 (2011)

[60] S. Bossuyt, *Optimized patterns for digital image correlation*, in *Imaging Methods for Novel Materials and Challenging Applications, Volume 3: Proceedings of the 2012 Annual Conference on Experimental and Applied Mechanics* (Springer, 2012), pp. 239–248